1-1-2013

Biomechanics of Porcine Renal Artery and the Development of A Replacment Vessel

Mohamed Gabr
University of South Carolina - Columbia

BIOMECHANICS OF PORCINE RENAL ARTERY AND THE DEVELOPMENT OF A REPLACEMENT VESSEL

by

Mohamed G. Gabr

Bachelor of Science
University of South Carolina, 2011

Submitted in Partial Fulfillment of the Requirements

For the Degree of Master of Science in

Biomedical Engineering

College of Engineering and Computing

University of South Carolina

2013

Accepted by:

Susan M. Lessner, Director of Thesis

Michael Sutton, Reader

Lacy Ford, Vice Provost and Dean of Graduate Studies

Dedication

For my late mother, Dr. Azza Sadek Ph.D.; father, Dr. Gamil Gabr M.D.; sister, Yasmine Gabr; and brother, Kareem Gabr

Acknowledgements

This project was funded by the South Carolina Project for Tissue Biofabrication NSF EPS-0903795 (SML, MAS), NIH 8P20 GM103444-04 (SML) and by NSF CMMI-1200358 (SML, MAS). A special thanks to Prof. Michael Sutton, Dr. Tarek Shazly Ph.D., Prof. Xiaomin Deng, and Dr. John Eberth Ph.D. for all of their help and support in completing my research. I would like to thank my colleagues Boran Zhou, Alexa Moreira, Ian Miller, John Johnson, Bilal Merei, and Lindsey Davis. I would like to thank Caughman Meat Plant for providing the tissue samples. I would also like to thank Dr. Scott Argraves and Sandy Klatt at the Medical University of South Carolina for providing the newly developed tissue constructs.

Abstract

Mechanical characterization of biological soft tissues is essential in the field of biomedical engineering. In this study several loading experiments have been performed to efficiently characterize the passive mechanical response of both native porcine renal arteries and newly developed tissue constructs. The first aim of these studies is to determine whether there is a difference in mechanical response between the main renal artery and its first branch. After fitting the bi-axial data to a Holzapfel-type constitutive model, the results show that there is no statistical difference between the model parameters for renal artery and the first branch. The only significant differences between these two vessels were the geometric parameters. The second aim is to characterize the response of newly developed tissue constructs during their development, since recent studies [3] have shown that they vary in strength over time during the culture process. Specifically, mechanical characterization tests for the tissue constructs used in these studies show a significant increase in elastic modulus and failure strength as culture time is increased from 7 days to 17 days. The uniaxial mechanical test data was fitted to a simple single invariant constitutive model to determine appropriate material parameters that could be used in future studies to predict the 3-D response of tubular constructs. The test data was also used to obtain the low and high strain elastic modulus for elastin dominant and collagen dominant phases. The incremental elastic modulus data is useful for comparison to published values for other tissues.

Table of Contents

List of Tables

List of Figures

INTRODUCTION

Cardiovascular disease (CVD) is the number one cause of death globally. Estimates by the World Health Organization state that over 17 million people die from CVD each year, which is roughly 30% of all global deaths [1]. For this reason, there is a strong interest in understanding how both the heart and arteries behave under physiological loading. It is also important to test healthy arteries for their material properties so that we can compare "normal" vessel response to the response of diseased vessels or replacement grafts. In this study, the initial focus is on the renal artery, which provides the kidneys with blood and nutrients. According to a 2013 study, 10% of American adults have some level of chronic kidney disease (CKD) and the incidence of CKD in people over 60 years old is over 20% [2]. One of the main causes of CKD is renal artery stenosis. This condition is caused by the formation of plaque within the renal artery, resulting in stiffening of the walls of the artery.

Unfortunately, there is a lack of data in the literature regarding the biomechanics of healthy renal arteries, limiting the amount of baseline data available for comparison with diseased arteries. Since the anatomy and structure of porcine and human renal arteries are similar, in this study porcine renal arteries are used. Data is obtained that describes the passive mechanical behavior of a healthy porcine renal artery for comparison to measurements obtained for the first branch renal artery. The data could be used to compare with other arteries while also serving as a target for design of

replacement renal artery grafts, while also answering the question of whether the same material model could be used for both the renal artery and its first branch.

As technology advances, better methods for fabricating tissues emerge, such as the novel tissue constructs being developed at the Medical University of South Carolina (MUSC) which have the potential to be used as a replacement vessel [3]. In a collaborative effort with MUSC, commercially available macroporous, gelatin microcarriers were seeded with human umbilical vein endothelial cells (HUVECs) and human aortic smooth muscle cells (HASMCs) and dispensed in molds made from agarose. HUVECs and HASMCs are both anchorage dependent cell types, indicating that they must attach to a surface to grow, with the gelatin microcarrier beads acting as a scaffold to seed the cells. The agarose molds are used because agarose is bio-inert and will not allow HUVECs or HASMCs to attach. These conditions allow for the HUVECs and HASMCs to attach only to each other. The result is creation of extracellular matrix and cell-to-cell bridging that results in a tissue construct that can withstand mechanical loading. In fact, recent histological studies provided by our collaborators show the presence of collagen and elastin in the tissue construct [3].

In order to determine whether recently developed constructs are appropriate for arterial replacement applications, the mechanical properties of constructs are characterized using uniaxial loading of ring-shaped specimens that have been in culture from 7 to 17 days. As shown in the results of these studies, increasing culture time to 17 days resulted in a significant increase in mechanical strength of the construct material.

CHAPTER 1

BIOMECHANICS OF PORCINE RENAL ARTERY

Tissue engineers have extensively studied the type of cells that should be utilized when developing replacement blood vessels, while also providing a list of criteria that the replacement vessel should meet. In a general sense, to say that one has effectively created a replacement, the replacement must effectively mimic the native artery not only biologically but also in its response to mechanical load. Though the mechanical responses of some arteries have been studied extensively, not all major arteries have been mapped out and described in terms of their biomechanical properties. In particular, the properties of renal arteries have not been actively studied, resulting in a paucity of experimental data. Since such baseline data is necessary for the development of replacement renal artery constructs, the work described herein presents the results from recent studies focusing on quantifying the behavior of porcine renal arteries.

Renal arteries provide blood and nutrients to the kidneys, which are high demand organs. It is important to determine how these arteries behave under physiological loading. For example, it is known that arteries experience significant axial stretch *in vivo* [4, 5]. Several authors have shown that the axial force needed to maintain an artery at its in vivo axial stretch does not change with transient cyclical pressurization over the normal range [4, 5, 6]. However, the axial force phenomenon noted above has not been reported for the porcine renal artery. Furthermore, the properties of the renal artery and its first branch have not been compared. In this study, the stress-strain response of renal

arteries is measured by subjecting both the primary and first branch renal arteries to a combination of internal pressured and axial tensile loads. The results of these experiments are highlighted in this report.

In this study, the axial stretch ratio where the axial force does not change with pressurization will be determined. This axial stretch ratio will be considered the "in-vivo" stretch ratio. Furthermore, the stress/strain response of renal arteries is measured by subjecting both the primary and first branch renal arteries to a combination of internal pressures and axial tensile loads. The resulting experimental data from pig renal arteries are used to validate a biomechanical model relating the specific axial force phenomenon of arteries to the predicted load-dependent average collagen fiber orientation [7]. By solving for the parameters of this biomechanical model for the renal artery and the first branch, comparisons can be made between the model parameters.

1.1 MATERIAL CHARACTERIZATION

Renal arteries are muscular arteries that branch from the abdominal region of the aorta and connect to the kidneys at a structure called the hilus. Most individuals have two primary renal arteries, one to supply the left kidney and one to supply the right kidney. As shown in Figure 1.1, each of these arteries will bifurcate into the anterior and posterior segmental arteries before entering the hilus. Oftentimes there are anomalies in the geometry. A renal artery might fork into two or three segmental arteries, and one of those may bifurcate once more before entering the hilus.

There can also be a supernumerary renal artery, which occurs when there are two renal arteries that branch off the aorta and go to the same kidney; a supernumerary renal artery is shown in Figure 1.2. Though both of these anomalies have been observed in our

dissections, our studies will focus on comparing the mechanical response of the main renal artery (without anomaly) and its first branch when subjected to mechanical loading.

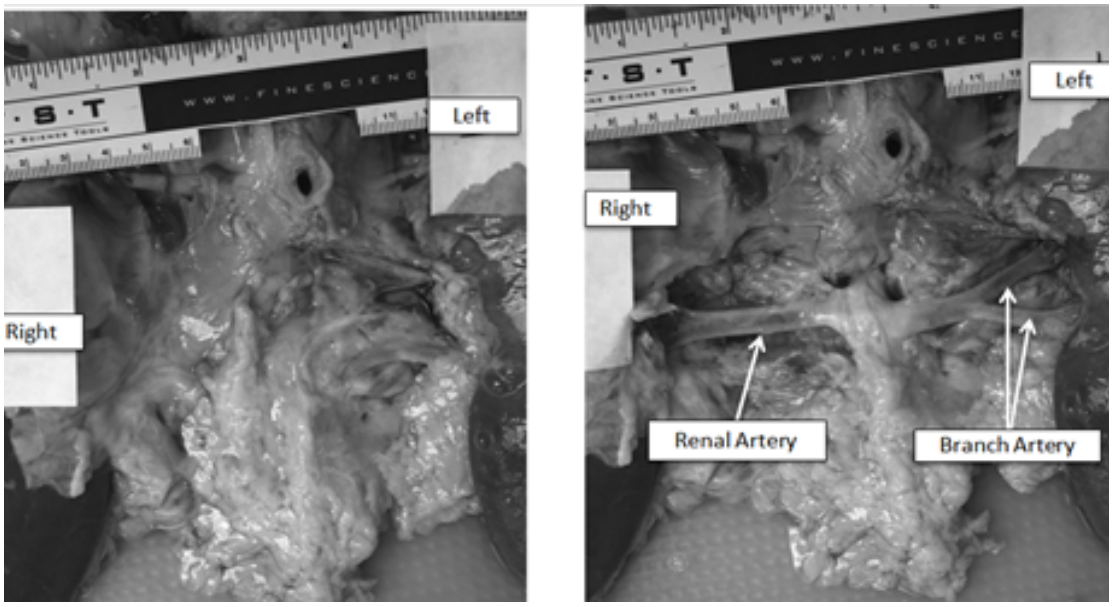

Figure 1.1 Porcine kidneys attached to aorta via renal artery: before (Left) and after (Right) adipose tissue removal

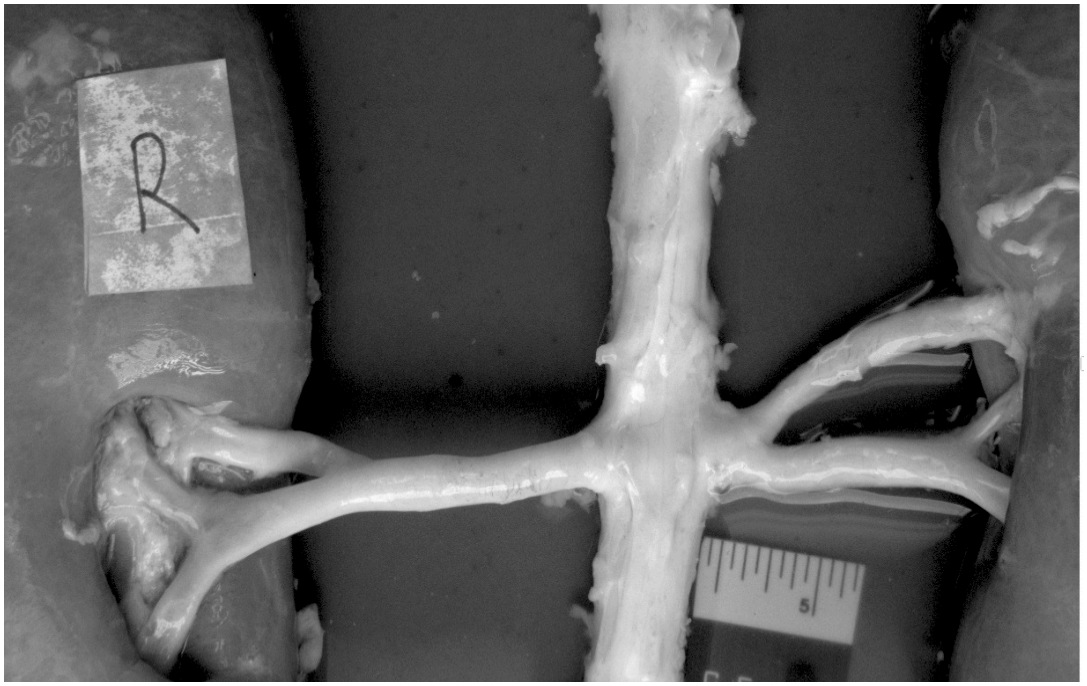

Figure 1.2 Renal artery in e*x vivo* state with surrounding tissues removed: Note the geometry of the vessels and the supernumerary left renal artery

Like all arteries, the renal artery consists of three anatomic layers. The innermost layer in direct contact with circulating blood is the intima. This layer provides negligible mechanical strength as it normally consists of a single sheet of endothelial cells (ECs) and their underlying basement membrane. The next layer is the media, primarily composed of smooth muscle cells, collagen, and elastin, which is considered the primary load-bearing layer in an artery [8]. The elastin is engaged at low strains (5-10%), and its elasticity helps the artery recoil quickly. It is believed that the network of collagen and elastin is responsible for the anisotropic behavior of the material, as well as the overall strength of the vessel. The outermost layer, the adventitia, is also composed of collagen and variable amounts of elastin but with the addition of adipose tissue (fat).

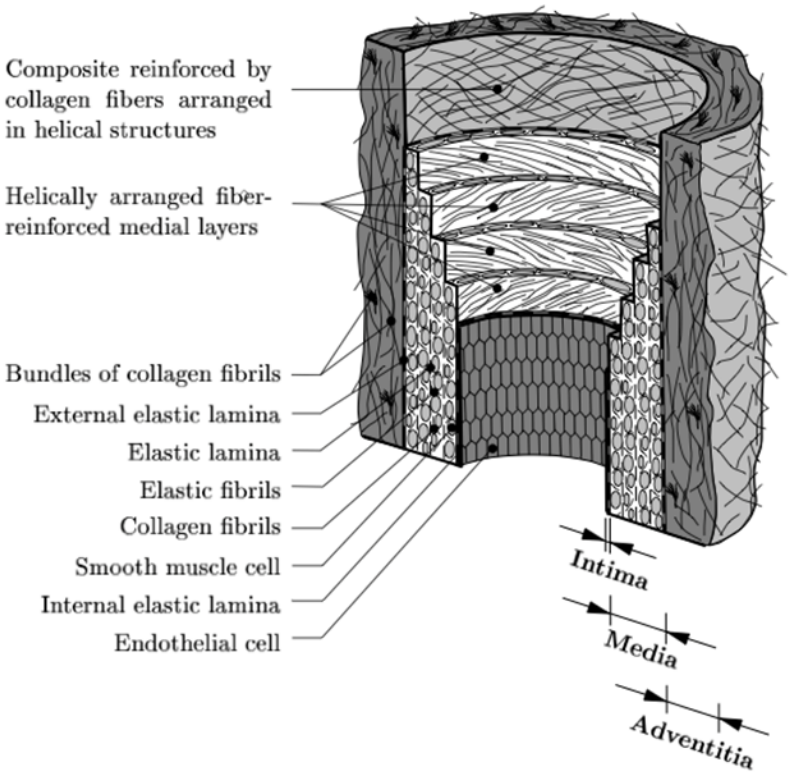

Figure 1.3 Schematic of artery by layers and composition (Adapted from [8])

Since the literature suggests that collagen and elastin are major bearers of load in arterial tissues, we investigated the collagen and elastin content of our specimens [9]. Paraffin sections of arterial segments were stained with Picrosirius Red and Verhoeff's stain to determine area percent of collagen and elastin, respectively, by image analysis (Figure 1.4).

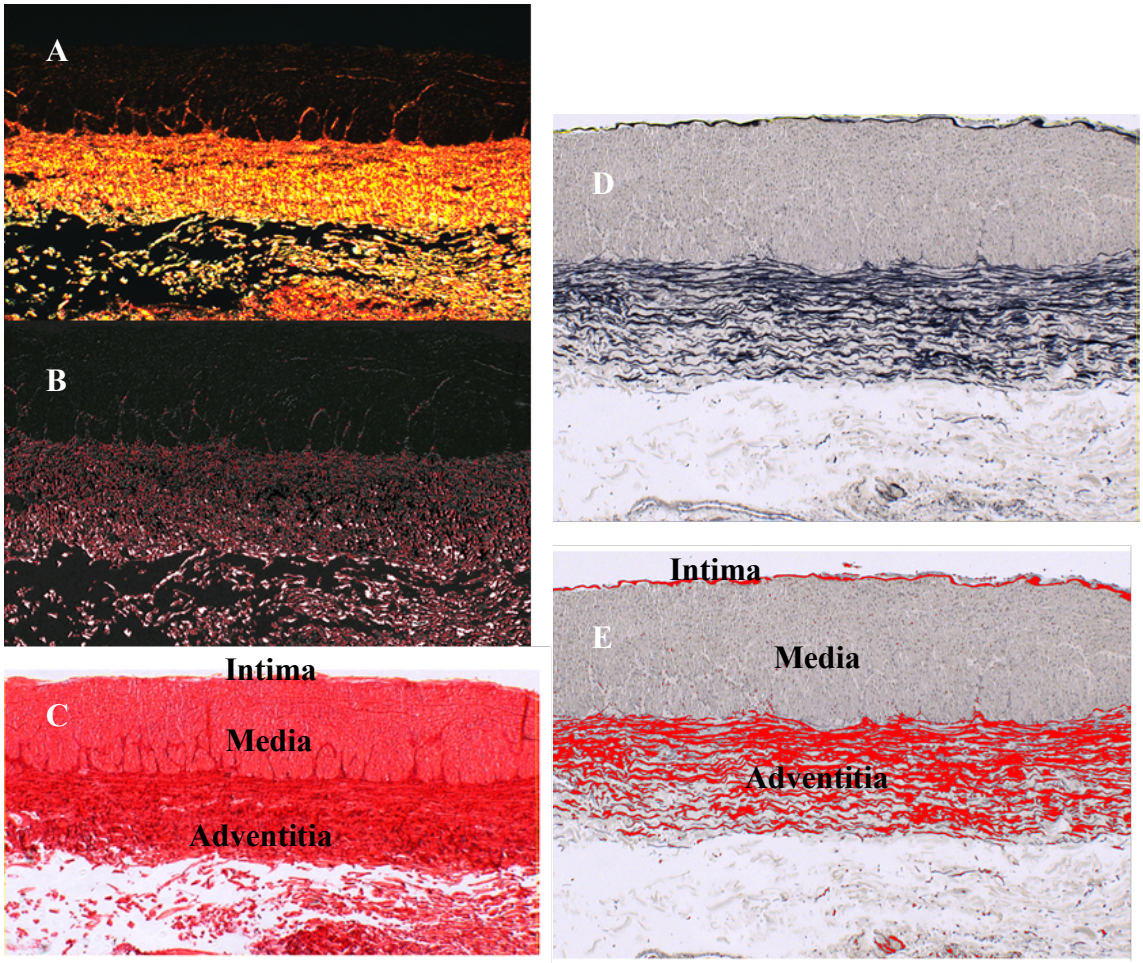

Figure 1.4 [Left] Picrosirius Red staining for collagen and [Right] Verhoeff's staining for elastin

As seen in Figure 1.4 A, the cross-polarized transmitted light microscopic image of stained collagen is yellow-orange on a black background, due to the birefringence of

collagen. By using the image analysis software, ImagePro, the pixels corresponding to collagen can be segmented from the image to measure the total area of collagen (Figure 1.4 B). Area percent was calculated by measuring the total area of collagen, dividing by the total area of the sample wall and multiplying by 100. The total area of the vessel wall is determined by measuring the area of red staining in the corresponding bright field image, as seen in Figure 1.4 C.

Determining the area fraction of elastin is similar to the procedure used for collagen. Figure 1.4 D shows a renal artery section stained with Verhoeff's stain to visualize elastin. Elastin stains blue-black on a grey background. The amount of elastin can be measured by determining the total black area, shown segmented in red in Figure 1.4 E. The total area of the sample wall is measured from the bright field image shown in Figure 1.4 D.

Results from our studies are shown in Table 1. As shown in Table 1, collagen and elastin content are not significantly different in both branch levels of the renal artery. Results from a 2 tailed t-test yielded P values larger than P=.05, which suggests that there are no major differences in collagen/elastin composition between the main renal and the first branch.

Table 1.1 Collagen and Elastin Content in Primary and First Branch Renal Artery Specimens

	Sample Number	% Collagen	% Elastin
Renal Artery	11	11.95 ± 0.25 %	9.03 ± 0.14 %
First Branch/ Segmental	4	11.38 ± 0.19 %	8.97 ± 0.04%

1.2 MECHANICAL TESTING

Pairs of porcine kidneys attached to intact abdominal aortic segments were acquired post-mortem from a local processing facility, Caughman's Meat Plant, Lexington, SC. Based on information provided by, Caughman's Meat Plant, the specimens were obtained from 2-3 yr old sows (weight range approx. 159-205 kg). After removal from the carcass, the arterial specimens remained immersed in phosphate buffered saline (PBS) solution until the mechanical loading process was completed; all experiments were performed within a few hours of tissue removal from the pig. When detaching the porcine renal artery and first branch artery specimens from the kidneys, the *in situ* axial and circumferential stretches were estimated through measurement of (a) the axial contraction of the artery specimen during removal and (b) the final outer diameter of the artery specimen after removal. The change in geometry associated with a typical excision of the renal artery specimens is shown in Figure 1.5.

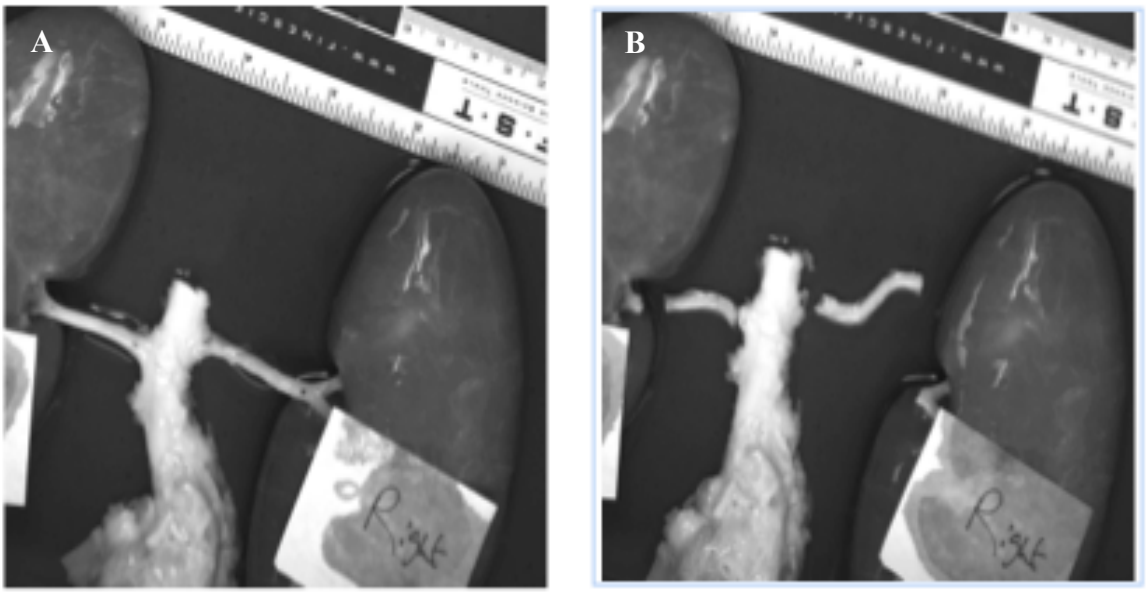

Figure 1.5 Extraction of renal artery specimens for in-situ measurement of axial and circumferential stretches

To obtain an estimate for the *in situ* axial stretch, markers were placed on the renal artery specimen at a few locations along the length. Then, with a ruler in the field of view, a camera was placed perpendicular to the renal artery and an image of the specimen and ruler was acquired prior to excision. After excision, another image was acquired of the specimen without altering the camera settings and with a ruler again in the field of view. Using these images, post-processing was performed to obtain estimates for the axial stretch ratio, λ_a, between the markers, which is defined as follows;

$$\lambda_a = \frac{L_{af}}{L_{a0}} \qquad \text{Eq 1.1}$$

L_{af} is the in situ axial length of the vessel before contraction as seen in Figure 1.5A and is considered to be the "stretched" state. L_{a0} is the length of the vessel after excision and axial contraction, and is considered to be the "traction-free" or "load-free" length. This is considered to be the undeformed state of the specimen. Any change in axial length greater than the initial "load-free" length results in axial stretch, λ_a. The measurement of in-situ axial stretch ratios is used in our studies to determine the amount of strain to apply during testing.

To obtain an estimate for the in situ circumferential stretch ratio, λ_c, the same images were again post-processed. Defining the circumferential stretch ratio, λ_c, by;

$$\lambda_c = \frac{C_{af}}{C_{ao}} \qquad \text{Eq 1.2}$$

Where C_{af} is the circumference of the vessel before excision and C_{a0} is the circumference of the vessel after excision. C_{a0} is determined when the vessel has reached the "load-free" length. Due to axial contraction, $\lambda_c < 1$ for in situ circumferential stretch ratios. During pressure loading, $\lambda_c > 1$. The value for λ_c is determined by measuring the

diameter of the vessel at several clearly identifiable locations along the vessel before and after excision, through post-processing of the images.

In addition to the in-situ deformations that an artery experiences, studies have shown that the excised, contracted artery specimens continue to have internal circumferential "residual" strains. To quantify this strain, the common practice is to remove ring specimens from the renal arteryand slice across the thickness of each ring specimen to open due to the removal of the residual circumferential stresses. After slicing through the thickness, the specimen is allowed to relax for 30 minutes while in solution. This process is shown in Figure 1.6.

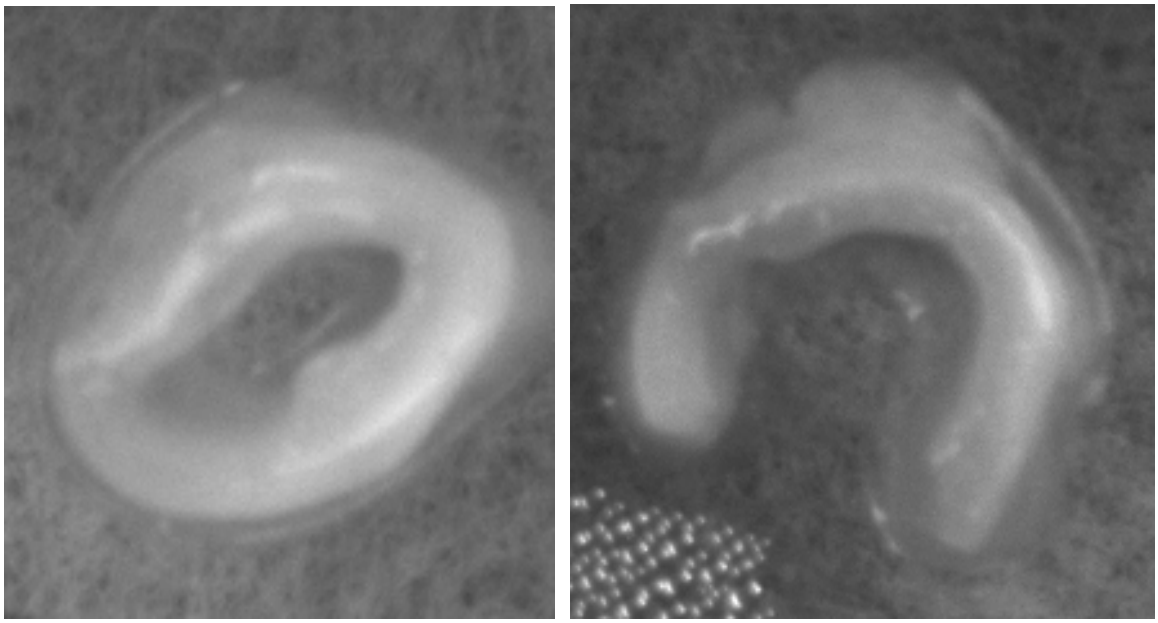

Figure 1.6 Ring specimen from renal artery before [Left] and 30 min after [Right] slicing across thickness into open sector

To quantify the residual strain, the opening angle Φ_o defined graphically in Figure 1.7 is measured after 30 minutes. Along with vision-based measurements, this angle is used to estimate the final outer circumference of the opened ring specimen so that the residual circumferential strain can be determined.

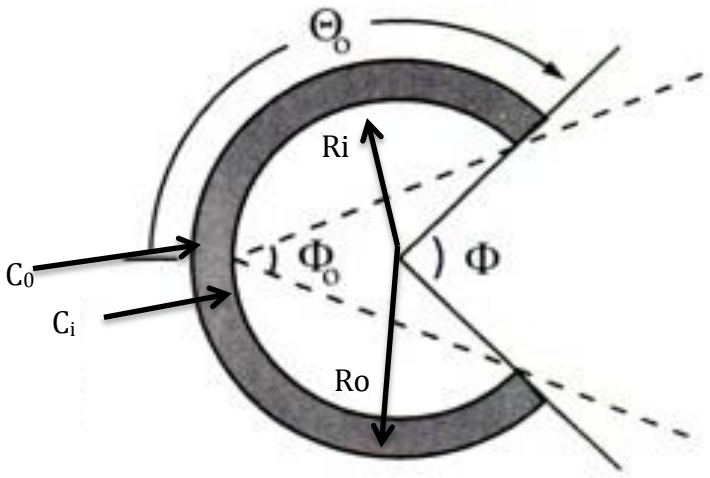

Figure 1.7 Schematic defining opening angle (Adapted from [8])

In this study, the opening angle, Φ_0, was determined by image analysis. Three measurements of Φ_0 were taken manually and averaged using ImagePro. Two lines (the dotted lines in figure 1.7) were manually drawn and the angle between then was considered the opening angle. The opening angle can also be solved for geometrically. As seen in Figure 1.7:

$$\Phi = 2(\pi - \Theta) \qquad \text{Eq.1.3}$$

$$\Phi_0 = (\pi - \Theta_0) \qquad \text{Eq. 1.4}$$

$$\Theta_0 = (\pi - \Phi_0) \qquad \text{Eq. 1.5}$$

The outer circumference, C_o, and the inner circumference, C_i, can be written as functions of the inner radius, R_i, outer radius, R_o, and the opening angle, Φ_0, as seen below in Eq. 1.6 and 1.7;

$$C_i = 2\Theta_0 R_i = 2(\pi - \Phi_0)R_i \qquad \text{Eq. 1.6}$$

$$C_o = 2\Theta_0 R_o = 2(\pi - \Phi_0)R_o \qquad \text{Eq. 1.7}$$

The thickness, H, can be written as the difference between the outer and inner radius, which can be seen in Eq. 1.8;

$$R_o - R_i = H \quad \text{Eq. 1.8}$$

The cross sectional area of the open ring specimen is defined as:

$$A = \frac{H(C_o + C_i)}{2} \quad \text{Eq. 1.9}$$

The aim of these equations is to be able to calculate the opening angle based on the geometry. Subtracting Eq. 1.6 from Eq. 1.7 leads to the following form;

$$C_0 - C_i = (2\pi - 2\Phi_0)(R_o - R_i) \quad \text{Eq. 1.10}$$

Substituting Eq. 1.8 into 1.10 gives rise to the following equation;

$$C_0 - C_i = (2\pi - 2\Phi_0)H \quad \text{Eq. 1.11}$$

After algebraic manipulation, Φ_o is defined by:

$$\Phi_0 = \pi - \frac{C_0 - C_i}{2H} \quad \text{Eq 1.12}$$

where C_0 is the outer circumference of the open ring specimen, C_i is the inner circumference of the sector, and H is the thickness of the specimen. This calculated value was found to have a high degree of variability in comparison to the measurements made by manually measuring the opening angle. The reason for the high variability in the results is due to the irregularity of the inner and outer sector arc length. There is a connective tissue on the outer arc length also increases the difficulty of accurately measuring the outer arc length.

Once the initial geometric measurements were obtained, the remaining artery specimens were prepared for combined pressurization and axial load experiments. All experiments were carried out on a Bose Electroforce Biodynamic 5100 Test Bench (Bose, Eden Prairie, MN) shown in Figure 1.8 and Figure 1.9. The Bose Test Bench

includes (a) 22N load cell, (b) micro-pump capable of delivering 102ml/min, (c) catheter-mounted pressure sensor with a range of 0-300mm Hg, (d) actuator that can produce a total displacement of 13mm, (e) environmental chamber to maintain hydration of the arterial specimens and (f) Bose software to control the entire mechanical loading process.

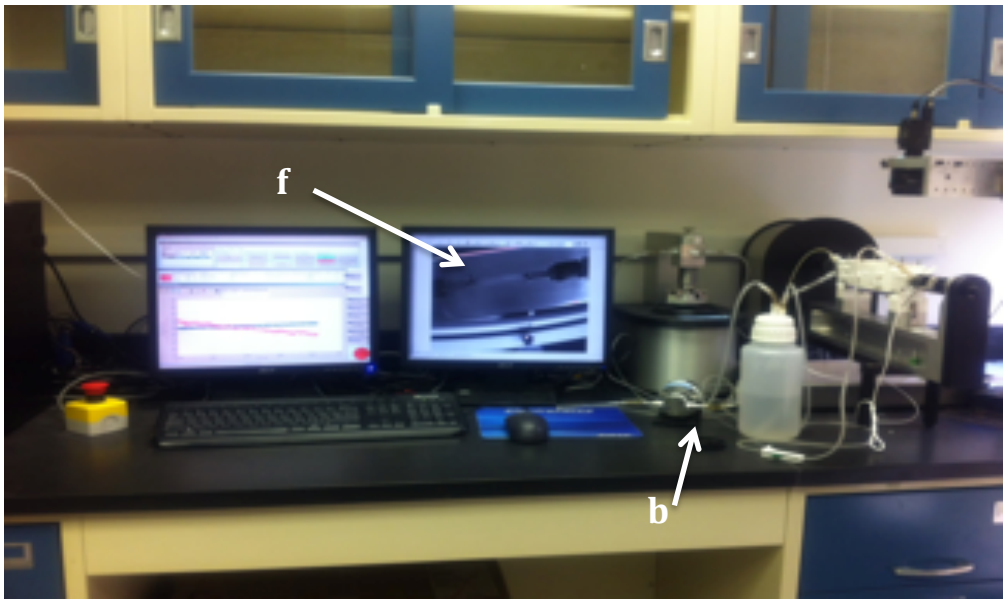

Figure 1.8 Bose 5200 Biodynamic Test Bench and components

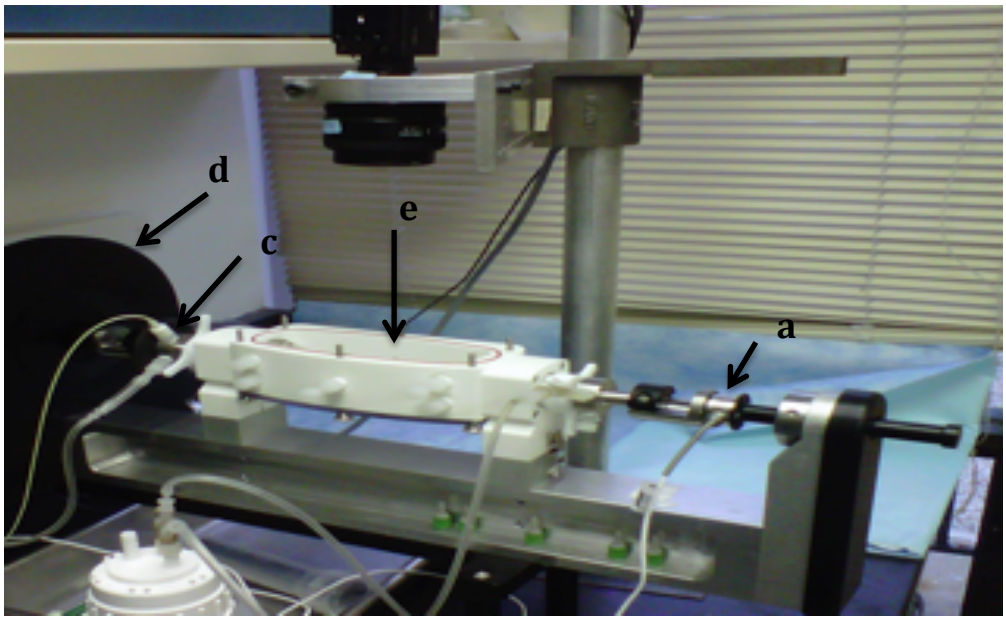

Figure 1.9 Close up of test bench and components

A typical renal artery specimen mounted in the test fixture is shown in Figure 1.10.

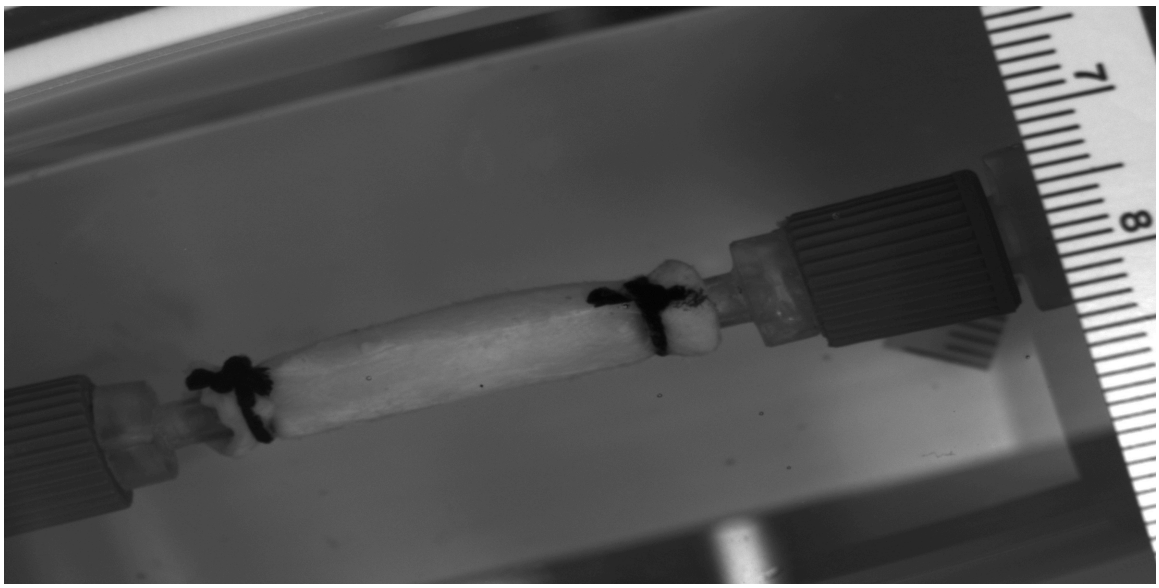

Figure 1.10 Renal artery specimen in test fixture for combined pressure-axial loading experiment

To perform the experiments, each arterial specimen was mounted onto hollow cylindrical, barb-ended Luer stubs (McMaster-Carr) using 3-0 silk sutures. After the specimen was tied onto the Luer stubs using the suture material, the stub-artery combination was attached to the end fixtures of the Bose Test Bench and immersed in a bath of 1 X PBS solution within the environmental chamber. The specimen was immediately perfused internally with the same solution at room temperature and perfusion was maintained throughout the loading process. The length of the specimen (between the 2 sutures) at zero load is the initial undeformed length or traction-free length, as measured previously. Prior to initiating the experiments, each arterial specimen is pre-conditioned mechanically by pre-stretching to an axial strain of 3.5% for three cycles. In our experiments, we have found that a preconditioning stretch of 3.5% of the

traction-free length was sufficient to obtain consistent results while minimizing damage to the specimen.

Experiments were performed in axial displacement control and pressure control. The specimens were subjected to pressure loading over the range 20mmHg $\leq$ P $\leq$ 140mmHg and axial stretch ratios encompassing the range of $1.00 \leq \lambda_z \leq 1.25$. To determine the axial stretch ratio, the initial undeformed length was defined to be the length of the specimen between the sutured ends when the axial load is zero. During the displacement control tests, the pressure was held constant (P=20, 60, 100 or 140mmHg) and axial displacement was applied at a constant rate until the maximum stretch ratio, λ_z=1.25, was reached. During the pressure control tests, the axial stretch ratio was held constant and the pressure was gradually increased from the initial 20mmHg until the maximum pressure of 140mmHg was reached. The pressure was held constant briefly while images were acquired.

During the mechanical loading process, the deformed outer diameter and length of the specimen were determined at each loading step by analyzing images of the specimen. In this study, all images were acquired using a Grasshopper 50S5M 5.0 megapixel CCD camera (Point Grey, Richmond, BC) with a 28mm Nikon lens. Image acquisition was performed using Vic-Snap 2010 Software (Correlated Solutions, Columbia, SC). The images were analyzed using ImagePro Plus 7 image analysis software (Media Cybernetics, McClean, VA) to determine the average deformed diameter in the central region and the deformed length. To obtain the axial and circumferential stretch ratios during the loading process, the procedures outlined above for measurement of *in situ* dimensions are essentially repeated at each load step to determine the current diameter

and current length at selected marker positions along the length. These were then used with the reference values to obtain an average axial stretch ratio and average circumferential stretch ratio.

Ten segments of pig renal arteries from five different pigs were tested using this protocol. Five segments came from the right renal artery (RRA) of the pigs, one from the left renal artery (LRA) and four others came from the left segmental artery (LSA) of the pigs, which is the first branch of the renal artery entering the kidney.

2.3 MECHANICAL CHARACTERIZATION

The force-displacement data was analyzed to determine stress/strain behavior of the material. The Cauchy stress was determined assuming constant density and constant volume (V).

$$V = A_c * L_f = A_{c0} * L_0 \quad \text{Eq. 1.13}$$

where A_c is the current cross sectional area, L_f is the current length during the experiment, A_{co} is the initial cross sectional area at the load free length, L_0. A_c can be written as;

$$A_c = \pi({r_o}^2 - {r_i}^2) \quad \text{Eq 1.14}$$

where r_o is the current outer radius that is measured experimentally and r_i is the current internal radius that is solved for algebraically, the volume can also be written as;

$$V = \pi({r_o}^2 - {r_i}^2)L_{a0} \quad \text{Eq. 1.15}$$

Solving for r_i

$$r_i = \sqrt{{r_o}^2 - \frac{V}{\pi * L_{a0}}} \quad \text{Eq. 1.16}$$

Substituting Eq. 1.13 into Eq. 1.16 gives the form;

$$r_i = \sqrt{{r_o}^2 - \frac{A_c * L_{af}}{\pi * L_{a0}}} \quad \text{Eq. 1.17}$$

Because the current cross sectional area cannot be measured while conducting the experiments, we can manipulate Eq. 1.17 so that it is a function of variables that are either measured before running the experiment (H, R_i, Φ_0) , or variables that are measured during running the experiment (r_o and λ_a). Substituting Eq. 1.6, 1.7, and 1.8 into Eq. 1.9 leads to the following form;

$$A = \frac{H(C_0 + C_i)}{2} = \frac{H(2\pi - 2\Phi_0)(R_o + R_i)}{2} = \frac{H(2\pi - 2\Phi_0)\left((R_i + H) + R_i\right)}{2} \quad \text{Eq. 1.18}$$

Simplifying Eq. 1.18 leads to the following equation;

$$A = H(\pi - \Phi_0)(2R_i + H) \quad \text{Eq. 1.19}$$

Substituting Eq. 1.17 into Eq. 1.19 gives;

$$r_i = \sqrt{{r_o}^2 - \frac{H(\pi - \Phi_0)(2R_i + H)L_{af}}{\pi * L_{a0}}} \quad \text{Eq. 1.20}$$

Substituting the stretch ratio, Eq. 1.1, into Eq. 1.20 gives rise to the final form of the inner radius;

$$r_i = \sqrt{{r_o}^2 - \frac{H(\pi - \Phi_0)(2R_i + H)}{\pi * \lambda_a}} \quad \text{Eq. 1.21}$$

Now that all the equations are defined using variables that are easily measured experimentally, analysis on the sample can be completed. The wall force is written as;

$$F_W = F_m + \pi P {r_i}^2 \quad \text{Eq. 1.22}$$

where F_m is the measured load from the load cell and r_i is the calculated inner radius. The axial stress is defined using the following equation;

$$\sigma_z = \frac{F_W}{\pi({r_o}^2 - {r_i}^2)} \quad \text{Eq. 1.23}$$

Assuming thin walled vessels, the circumferential Stress is calculated as follows;

$$\sigma_\theta = \frac{Pri}{H} \qquad \text{Eq. 1.24}$$

The circumferential Stretch Ratio is calculated as;

$$\lambda_\theta = \frac{2\pi(r_o + r_i)}{C_0 + C_i} \qquad \text{Eq. 1.25}$$

Using these equations with measured axial force, applied pressure and measured geometric parameters from image analysis, representative axial stress-axial stretch ratio curves are presented below in Figure 1.11 and 1.12.

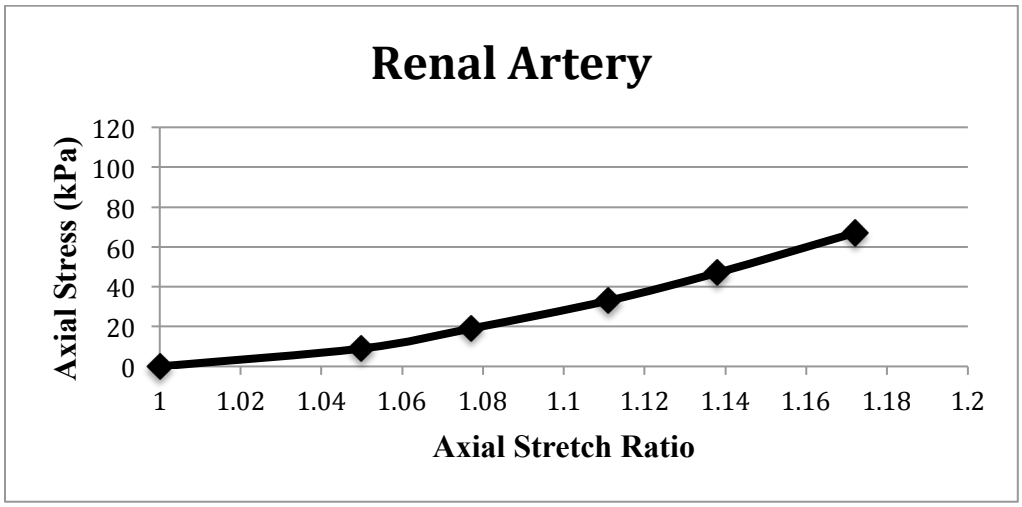

Figure 1.11 Representative axial stress-axial stretch ratio for renal artery

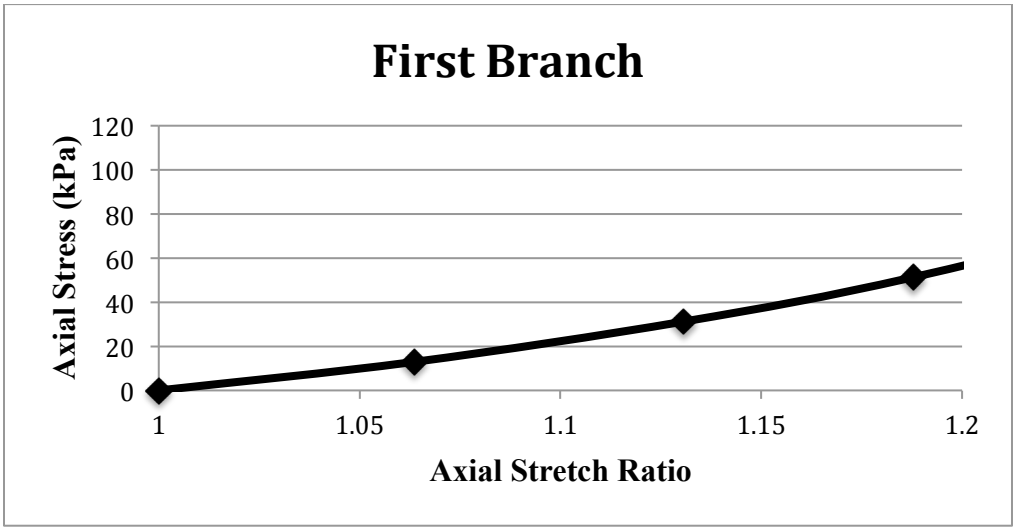

Figure 1.12 Representative axial stress-axial stretch ratio for first branch

Representative force-pressure curves as a function of axial stretch ratio can be seen below in Figures 1.13 and 1.14.

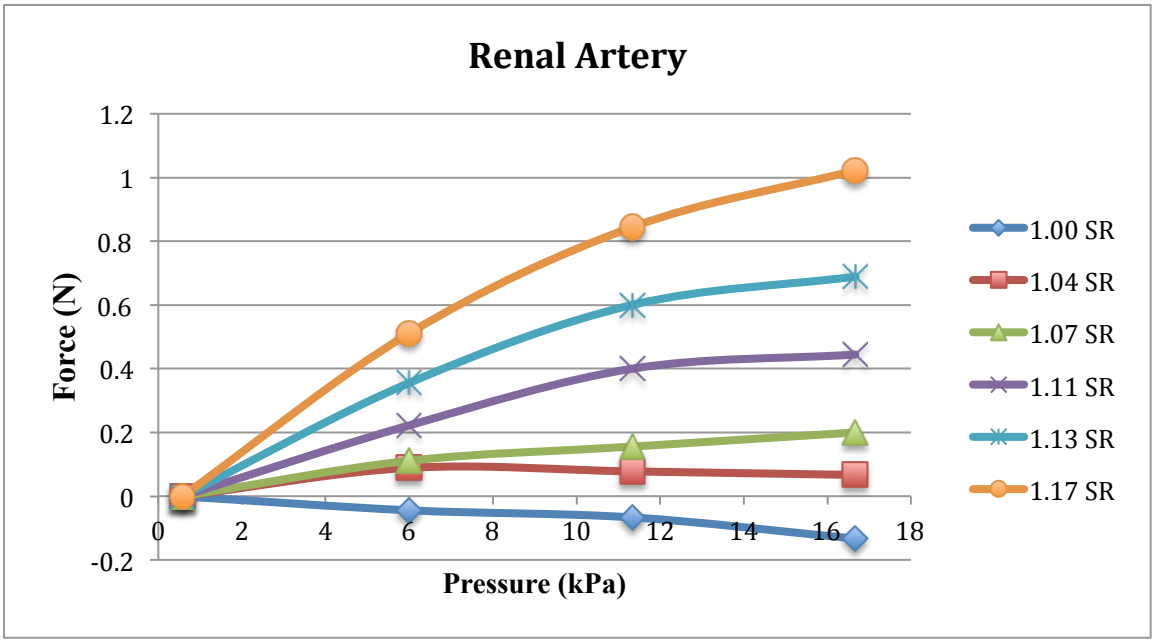

Figure 1.13 Representative force- pressure curves as a function of axial stretch ratio (SR) for renal artery

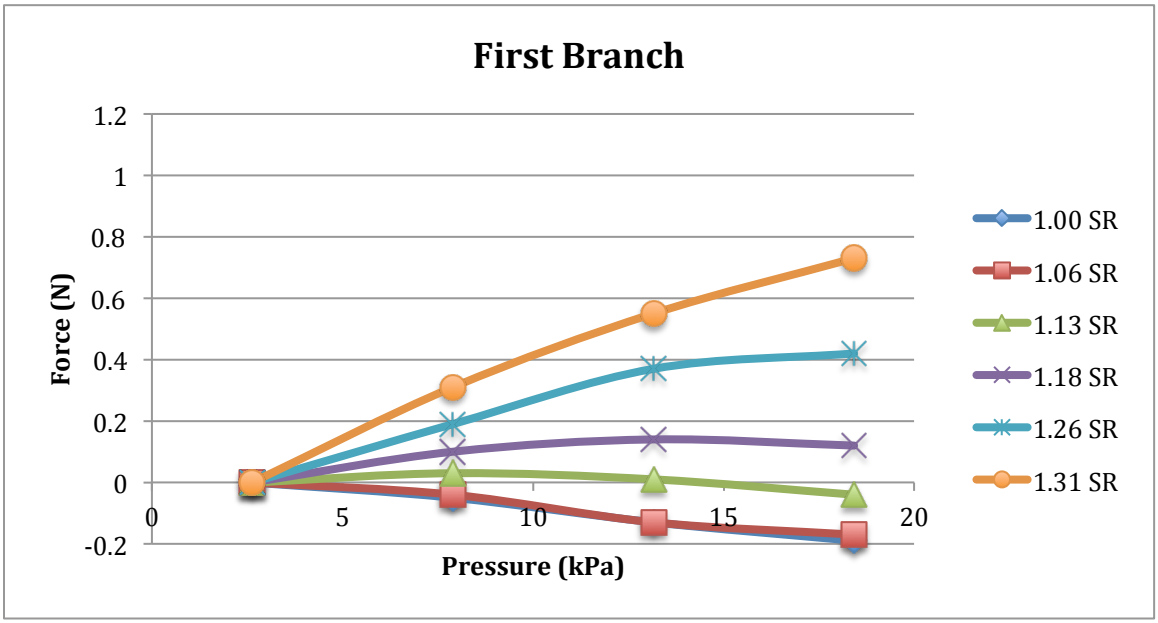

Figure 1.14 Representative force-pressure curves as function of axial stretch ratio (SR) for first branch of renal artery

Representative circumferential stress-circumferential stretch ratio curves are presented below in Figures 1.15 and 1.16

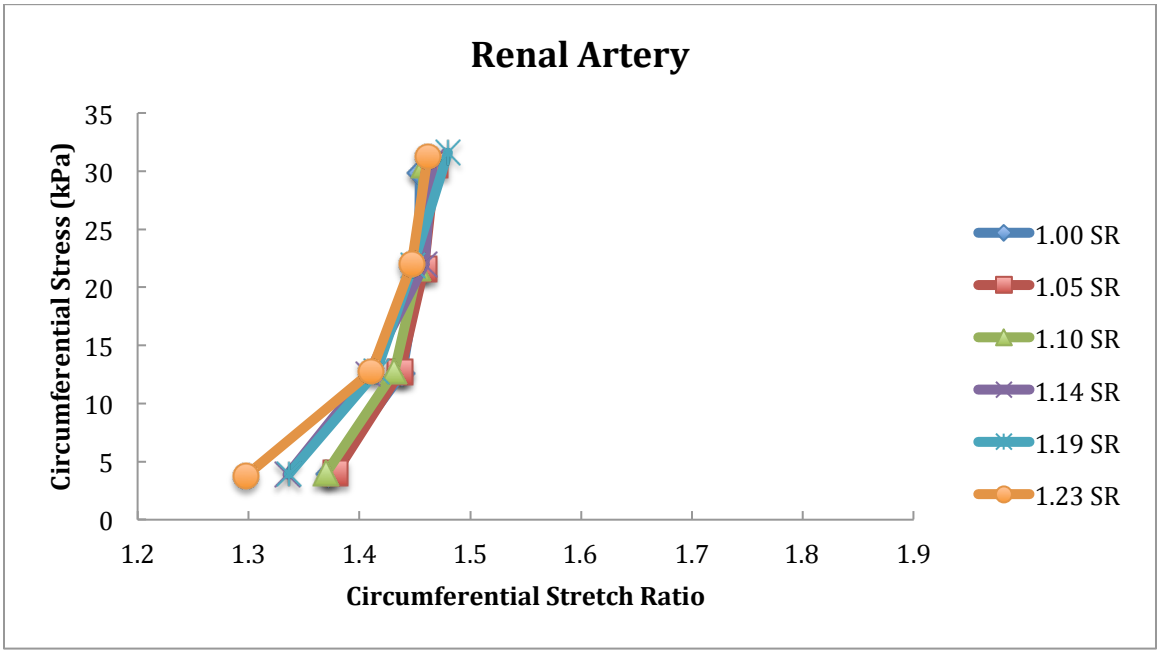

Figure 1.15 Representative circumferential stress-circumferential stretch ratio curves as a function of axial stretch ratio (SR) for renal artery

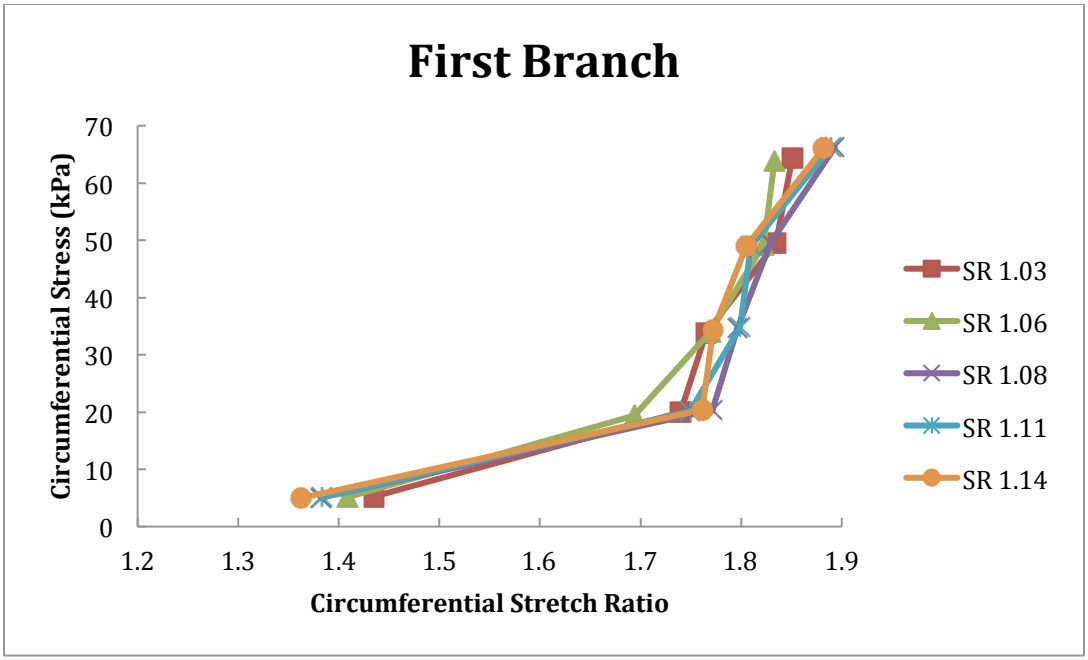

Figure 1.16 Representative circumferential-circumferential stretch ratio curves as a function of axial stretch ratio (SR) for first branch of renal artery

Using Figures 1.11 to 1.16, multiple conclusions can be presented. First, when comparing the axial stress-axial stretch ratio curves in Figure 1.11 and Figure 1.12, one can see that for any given axial stretch ratio, the axial stress is greater in the renal artery than in the first branch. This indicates that the renal artery is subjected to greater stresses than the first branch, given the same stretch ratio, which means to minimize stress, the renal artery should be at a lower "in-vivo" stretch ratio relative to the first branch. This prediction was confirmed as we saw that the "in-vivo" stretch ratio was greater for the first branch than for the renal artery in Figures 1.13 and 1.14.

Secondly, the slope of the axial stress- axial stretch data for the renal artery is greater than that of the first branch, indicating that the renal artery has a stiffer response to axial stretch than the first branch.

Thirdly, when comparing the axial load response to change in luminal pressure at different axial stretch ratios (Figures 1.13 and 1.14), it is noted that the results are similar to typical experimental F-P curves for arteries that have been reported in many scientific papers [5, 6, 9, 11]. Inspection of the data in Figs 1.13 and 1.14 shows that the slopes of the F-P curve vary at different stretch ratios. However, there is always a stretch ratio such that a change in pressure results in no change in axial load (dF/dP=0). The axial stretch ratio where dF/dP=0 corresponds to a predicted "*in-vivo* stretch ratio", since at this stretch ratio the forces in the vessel are minimized [4, 5, 6, 7, 10]. In these experiments, the predicted "*in-vivo* stretch ratio" was greater in the first branch than in the renal artery; the predicted "*in-vivo*" axial stretch ratio for the first branch was 1.2 and 1.07 for the renal artery.

In comparing the circumferential-circumferential stretch ratio curves (Figure 1.15 and 1.16), one can deduce that circumferential stress-circumferential stretch ratio response was independent of axial stretch ratio. In this test, the internal luminal pressure was increased while the outer diameter was measured at different axial stretch ratios. For any given circumferential stress, the circumferential stretch ratio was greater for the first branch than the renal artery. The increased circumferential stretch ratio suggests the first branch was more distensible than the renal artery.

The mechanical test data presented above was used to identify parameters in an adopted 4-fiber family nonlinear elastic constitutive model [7]. The model had 8 parameters to be determined (listed below).

- the opening angle: Φ_0
- the orientation angle of helical fibers in the stress-free state: β_0
- the stiffness property of the helical fiber: $k_{\beta 1}$
- the exponential stiffening coefficient of the helical fibers: $k_{\beta 2}$
- the stiffness property of the axial fibers: k_{901}
- the exponential stiffening coefficient of the axial fibers: k_{902}
- the stiffness property of the circumferential fibers: k_{01}
- the exponential stiffening coefficient of the circumferential fibers: k_{02}

The axial force predicted by the model can be written in the following form;

$$\tilde{F}_z = \tilde{F}_0(\lambda_z) + \int_{r_i}^{r_o} 2\pi \left[k_{\beta 1} \lambda_z^2 \sin^2(\beta_0) \left(\lambda_{\beta_0}^2 - 1 \right) \exp\left(k_{\beta 2} \left(\lambda_{\beta_0}^2 - 1 \right)^2 \right) \right] r\,dr - P\pi r_a^2 \qquad \text{Eq.1.26}$$

where

$$\tilde{F}_0(\lambda_z) = 2\pi \int_{r_i}^{r_o} \left\{ k_{901} \lambda_z^2 \left(\lambda_z^2 - 1 \right) \exp\left(k_{902} \left(\lambda_z^2 - 1 \right)^2 \right) \right\} r\,dr \qquad \text{Eq 1.27}$$

Our experimental data would only allow for the first 6 of the listed parameters to be determined. The parameters and their estimated values are presented in Table 1.2. (modified from [7])

Table 1.2 Identified Model Parameters for Renal Artery and First Branch

	O.D (mm)	**L (mm)**	**H (mm)**	Φ_0 **(deg)**	$k_{\beta 1}$	$k_{\beta 2}$	β_0	k_{901}	k_{902}
MAIN RENAL	**7.77 +/- 1.05**	**16.49 +/- 5.86**	**1.51 +/- 0.44**	**142.6 +/- 87.4**	**1677 +/- 2686**	**3.12 +/- 5.32**	**39.5 +/- 30.2**	**42.0 +/- 45.4**	**8.53 +/- 10.8**
FIRST BRANCH	**5.09 +/- 0.64**	**12.56 +/- 4.27**	**1.13 +/- 0.12**	**85.5 +/- 30.7**	**94.82 +/- 72.8**	**2.49 +/- 1.86**	**47 +/- 28.3**	**34.6 +/- 37.9**	**19.4 +/- 35.1**

The parameters k_{901}, k_{902}, k_{01}, and k_{02}, should be identified with a separate axial tensile test at a controlled zero pressure before carrying out the other pressure control test. This separate test was not achieved during this study, which represents a limitation. To determine the k_{901} and k_{902}, axial load values at the beginning of each pressure control test when the pressure was zero were used and the values shown for k_{901}, k_{902} were obtained directly from this data. Once determined, the values were set to their mean values to determine the remaining four parameters. Despite this limitation, the model is

still able to predict the incremental variations of axial loads in arteries when pressures and axial stretches vary.

The traction-free outer diameter of the main renal artery is significantly greater that that of its first branch (segmental artery), 7.8±1.1 mm vs. 5.1±0.6 mm (two-tailed t-test, $P < 0.01$), as expected in a diverging, branched arterial tree. In addition, the arterial wall in the stress-free reference configuration is significantly thicker in the main renal artery than in the first branch vessel (1.5±0.4 mm vs. 1.1±0.1 mm, P=0.045, 1-tailed t-test). Measured opening angles were not significantly different between the main renal artery and the first segmental artery.

The identified values for all the parameters of this model are reported in Table 1.2. It should be noted that the small number of specimens and the large variability among samples did not allow us to identify any statistically significant differences in fitted parameters between the main renal artery and its first branch.

2.4 CONCLUSIONS

In these studies a methodology for (a) combined pressure-axial load experimentation and (b) determination of the in-situ axial stretch ratio and circumferential stretch ratio is presented. The methodology is applied to obtain quantitative measurements for porcine renal artery specimens. The results show that there is a difference in axial and circumferential stress response between the main renal artery and the first branch when subjected to the same combined tension-pressure loading.

Interestingly, the histological analysis of the test samples showed that there not a significant difference in elastin and collagen composition between the two types of vessels. Even though both types of specimens had similar collagen content, a potential

reason for the difference in mechanical behavior is believed to be variations in average collagen fiber angle, which will be quantified in both vessels in future work.

By fitting a 4-fiber family Holzapfel-type constitutive model to the measured response of the renal artery specimens, it was determined that these arterial specimens could be modeled using the parameters listed in Table 1.2. There is no statistical difference in constitutive model parameters for the renal artery and the first branch. We found that there are only statistical differences in geometric parameters. The model parameter, β_0, suggests that we should expect to see a higher average collagen fiber angle in the first branch than in the main renal artery.

CHAPTER 2

BIOMECHANICS OF A NEWLY DEVELOPED TISSUE CONSTRUCT

As noted in Chapter 1, understanding how soft tissues behave in response to mechanical loading is essential in the field of biomechanics. When a new tissue construct is fabricated, it is essential that experiments be performed with minimal measurement errors to quantify the material properties that could easily be embedded in appropriate mechanical response models.

Tissue engineered constructs which contain cells derived from the patient's body that are suitable for vascular replacement procedures is a goal in medical research [12]. Various approaches have been developed to fabricate blood vessels [13, 14, 15]. These include the use of tubular scaffolds manufactured from natural and synthetic biomaterials that are subsequently seeded with vascular cells to create living prostheses [16, 17]. An alternative approach that would facilitate cell-based fabrication of conduits comprised of vascular cells and extracellular matrix (ECM) constituents was developed by collaborators at the Medical University of South Carolina (MUSC) [3]. In this study, the mechanical responses of such constructs were tested both at multiple culture times and multiple culture conditions.

The investigators at MUSC used macroporous, gelatin microcarriers laden with human umbilical vein endothelial cells and aortic smooth muscle cells to develop a new tissue construct that could be used in applications of vascular reconstruction. These

microcarriers were dispensed into ring-shaped agarose molds and shown to adhere to form living tissue constructs after several days in culture. The ability of cellularized microcarriers to adhere to one another involved cellular and extracellular matrix bridging that included the formation of epithelium-like cell layers lining the luminal and ablumenal surfaces of the constructs and the deposition of collagen and elastin fibers. The ring-shaped tissues nominally behaved as elastic solids, with a uniaxial mechanical response that is qualitatively similar to that of native vascular tissues and consistent with their elastin and collagen composition. Linearized measures of the mechanical response of the fabricated tissues at both low and high strains were observed to increase with duration of static culture, with no significant loss of stiffness following decellularization. The findings highlight the utility of cellularized macroporous gelatin microcarriers as self-adhering building blocks for the fabrication of living ring-shaped structures.

In this study, experiments to quantify the mechanical behavior of ring-shaped constructs formed by self-adhering gelatin microcarriers cellularized with human endothelial cells (HUVECs) and human aortic smooth muscle cells (SMCs) are performed The ring-shaped biological tissue constructs are tested in uniaxial tension experiments. Parameters to be determined from the ring test are those employed in a single invariant model to be described in Section 2.3.

2.1 MATERIAL DEVELOPMENT

Microcarrier beads are 100–300 mm diameter spherical particles that allow attachment and growth of anchorage-dependent cells while in suspension culture [18]. Microcarrier beads are manufactured from natural and synthetic materials, including gelatin, collagen, dextran, glass, polyethylene and polystyrene. Variant forms of

microcarrier beads are macroporous, having large pores of tens of micrometers that provide additional areas for cells to attach and grow [19]. Microcarriers have been generally used for suspension tissue culture to produce high yields of anchorage dependent cells and their secreted products, but in recent years their utility in tissue regeneration and tissue engineering has emerged [20]. An additional benefit of the gelatin microcarriers used in such applications is that they degrade over time in vivo without eliciting an inflammatory reaction [21].

Here, our colleagues at MUSC utilized vascular cell-containing macroporous gelatin microcarriers (Cultisphers) in conjunction with agarose molds to facilitate 3D tissue engineering of living ring constructs and evaluated their histological and material properties. Microcarrier beads ('Cultisphers') laden with co-cultured HUVECs/HASMCs were dispensed into tubular agarose molds. After several days in culture, the cellularized Cultisphers fused to create ring-shaped tissue constructs (4 mm diameter x ~2.5 mm long having a 2 mm bore).

Figure 2.1(a) shows the PEEK (polyetheretherketone) template used to generate ring molds in 6-well culture plates. Figure 2.1(b) shows that ring-shaped agarose molds are formed in a well of a 6-well culture plate. Figures 2.1(c) and (d) shown end views and side views, respectively, of a ring construct having an outer diameter of 4 mm, wall thickness of 1 mm, and height of 2.25 mm. Figures 2.1(e) and (f) are high magnification views of the boxed areas in panel (c), showing the inter-microcarrier bead material on the ablumenal (e) and lumenal (f) surfaces of the tubes (arrows).

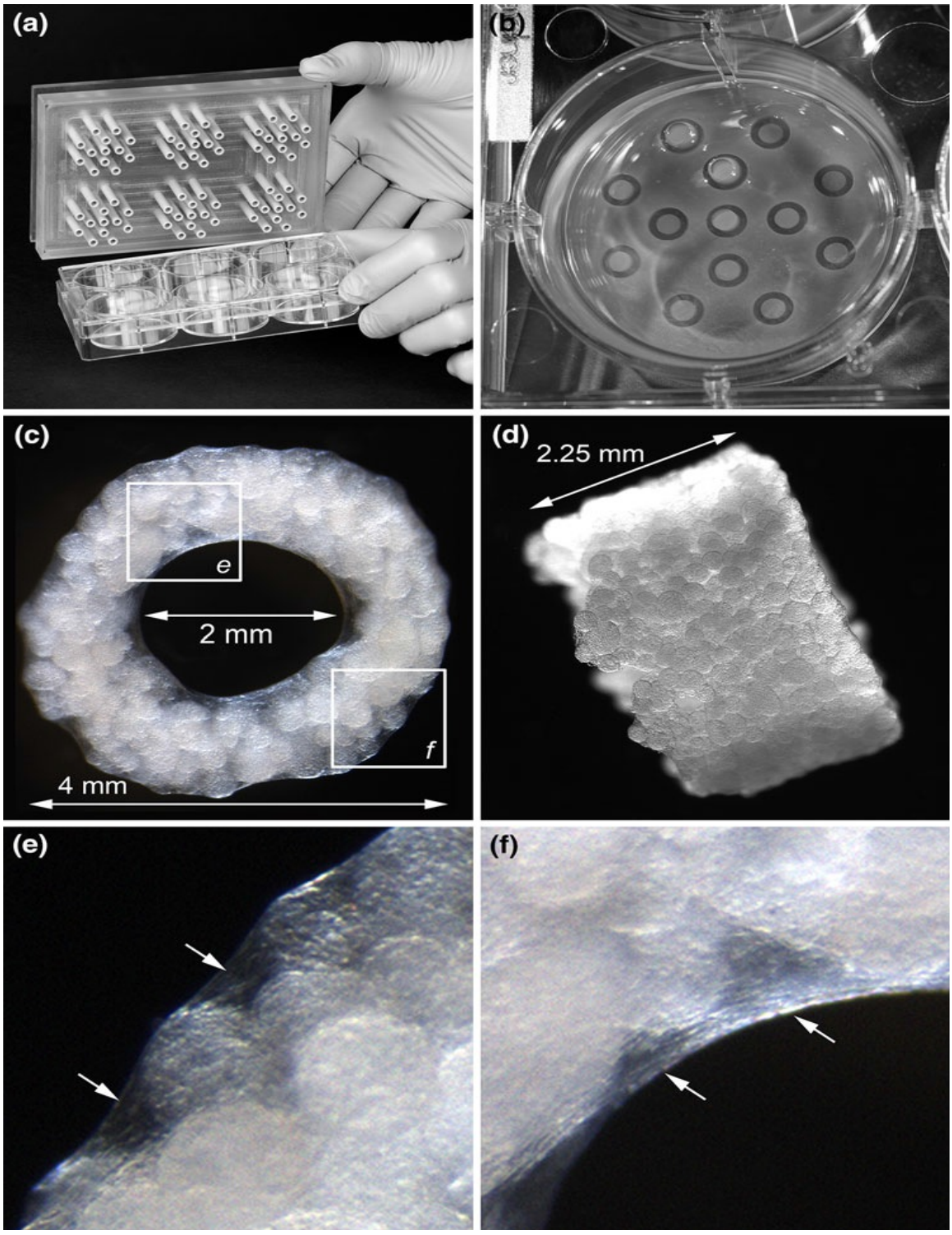

Figure 2.1 Cellularized Cultispheres placed in ring-shaped agarose molds assemble to form tissue ring constructs (Adapted from [3])

Histological studies were performed by our collaborators at the Medical University of South Carolina. Figure 2.2, panels A and B, show Masson's trichrome staining of frozen sections from ring-shaped constructs cultured for 17 days. Panel C and D show cross-polarized light images of Picrosirius Red (PSR) stained frozen sections from ring-shaped constructs cultured for 17 days. Arrows point to aligned fibrils, which based on their green/yellow birefringence in polarized light are immature collagen fibers.

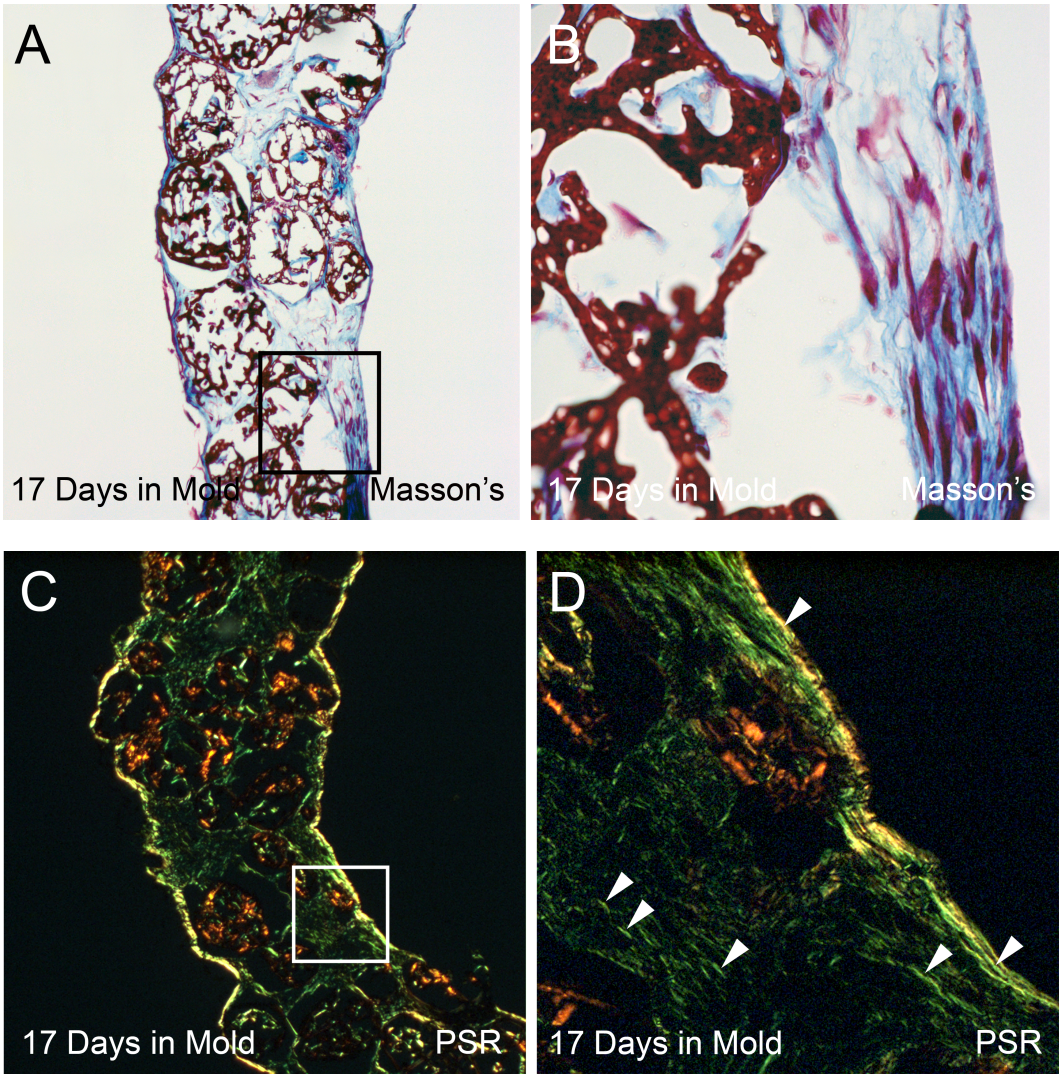

Figure 2.2 Collagen deposition in ring-shaped tissue constructs (Adapted from [3])

In figure 2.3, a ring-shaped construct was cut longitudinally to permit en face examination of the luminal surface. Nuclei were stained blue with Hoechst stain, and elastin (red) was visualized by immunohistochemistry using anti-elastin antibody. Panel B depicts the parallel orientation of anti-elastin-labeled fibrils shown in A.

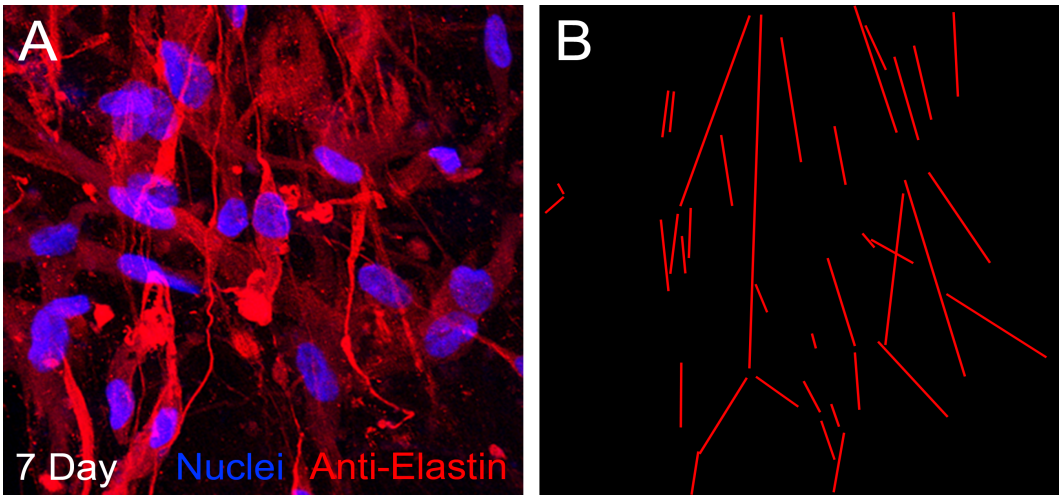

Figure 2.3 Anti-elastin stained whole mount of a ring-shaped construct cultured for 7 days. (Adapted from [3])

2.2 MECHANICAL TESTING

A uniaxial ring test was used to probe the passive mechanical response of ring-shaped constructs. To initiate mechanical testing, ring constructs were removed from agarose molds after 7, 12 and 17 days of culture and immediately secured onto horizontally oriented 25 gauge cannulas mounted to the upper and lower arms of a Bose Enduratec 3200 uniaxial mechanical tester (Figure 2.4 and 2.5)

Samples were kept hydrated with culture medium (1:1 mixture of EGM-2 and SMGM) while being mechanically preconditioned with four tensile displacement cycles up to 1.2 mm (20–25% strain) at a displacement rate of 0.01 mm/s (Figure 2.6). The sample showed minimal hysteresis during preconditioning (Figure 2.7). An identical fifth

cycle was then immediately performed, during which load data (50 points/s) was recorded by Wintest software.

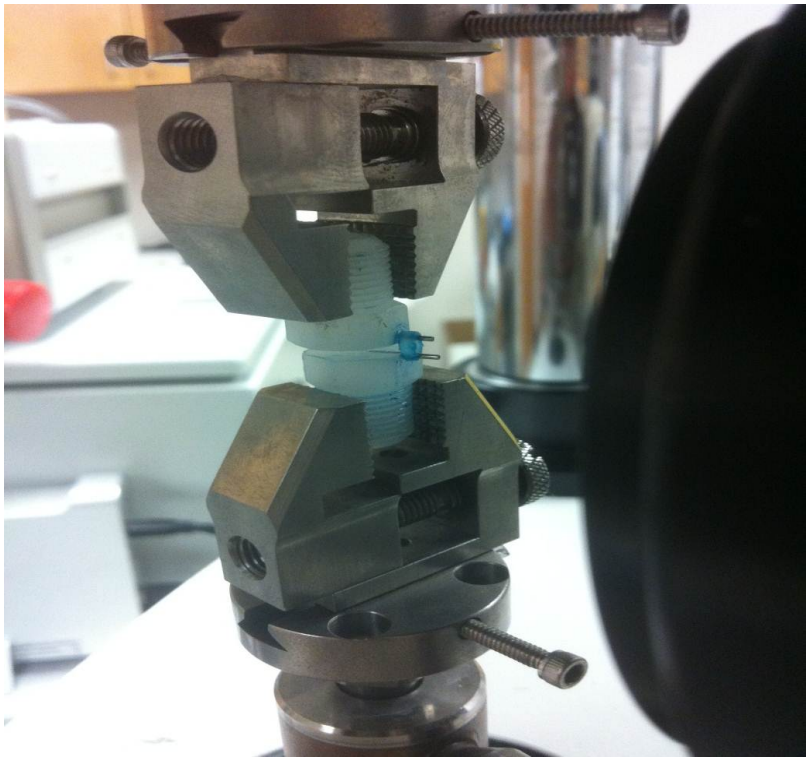

Figure 2.4 Testing a ring-shaped tissue construct on Bose 3200 uniaxial mechanical test bench

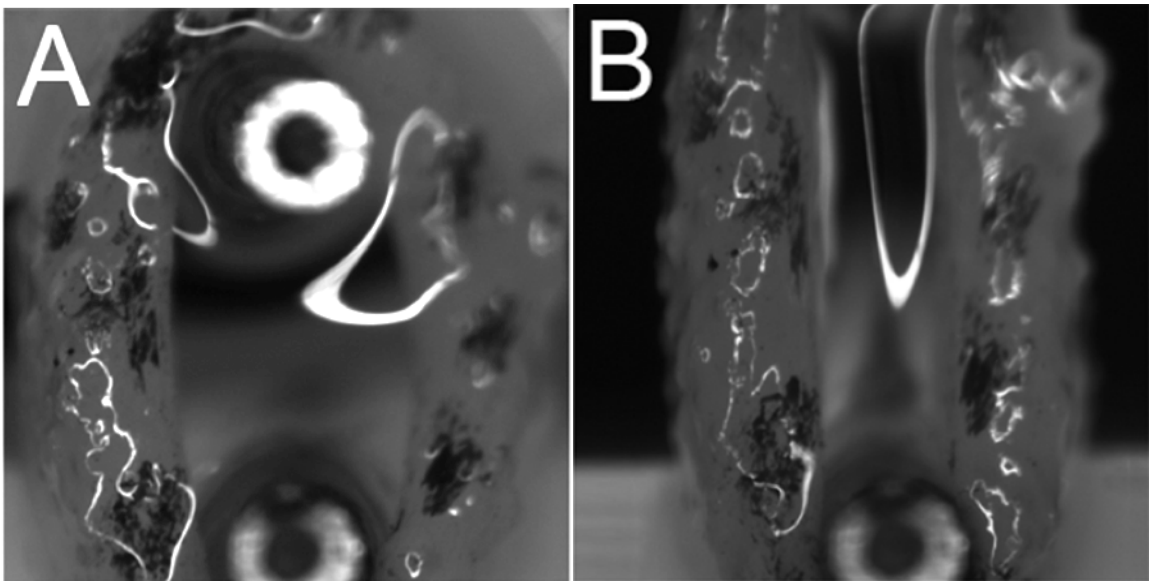

Figure 2.5 Constructs at (A) relaxed and (B) strained state

The white irregularly shaped lines in Figure 2.5 identify refraction at the edges of surface culture medium that was used to keep the sampled hydrated during the loading process. Region inside white lines is not used in image analysis due to distortions induced by the culture medium [25, 27, 28].

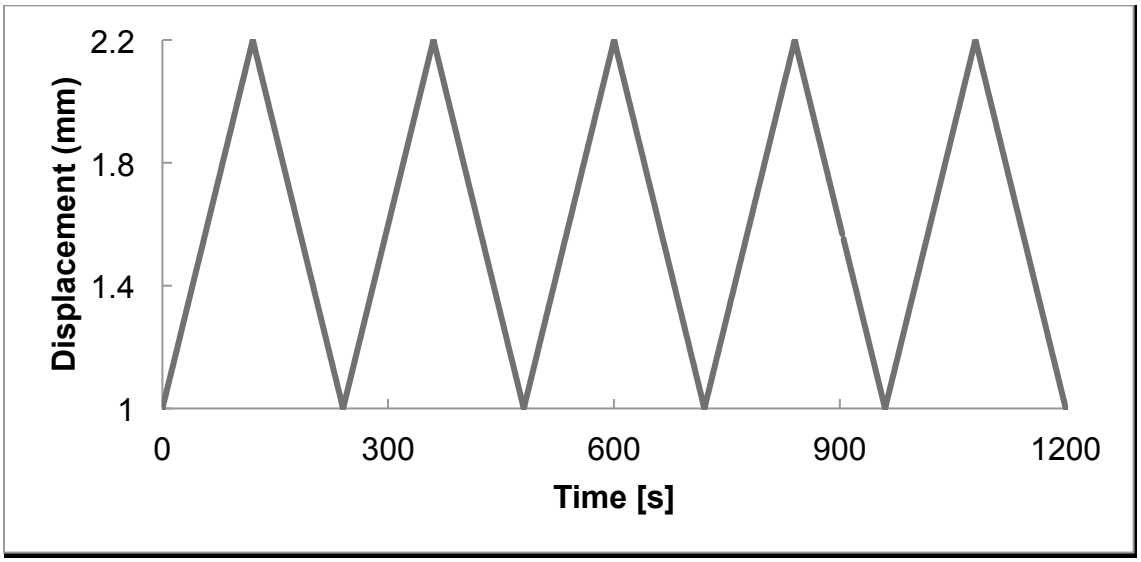

Figure 2.6 Programmed Bose actuator displacement for uniaxial tension experiment in displacement control mode

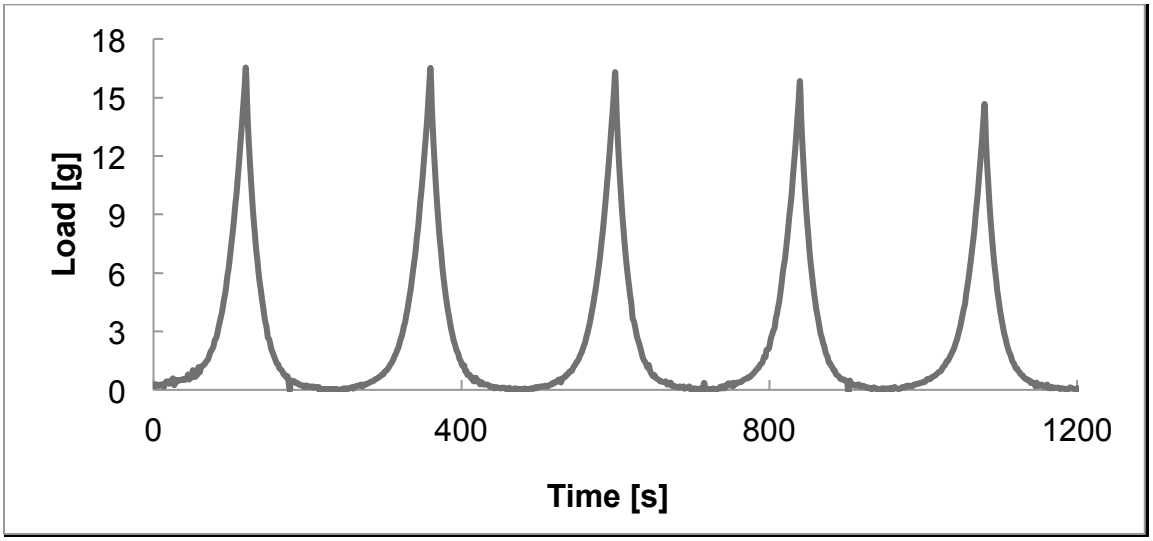

Figure 2.7 Specimen loading and unloading curves corresponding to displacement input in Figure 2.6, showing minimal hysteresis

An image-based technique was used to measure the local strain in the middle section of each sample. Immediately before sample mounting, blue tissue marking dye was applied by a fine tip applicator to create a dot pattern, as shown in Figure 2.8. A series of images was captured throughout testing using a Nikon SMZ-U light microscope and a Q-Imaging camera. Using ImagePro 5.1 to spatially calibrate the image, the vertical distances between the dots were calculated to facilitate measurement of local strain. The vertical distance measurement was determined using point tracking as a digital image correlation technique. Due to limitations in total viewing area, a ruler could not be placed to calibrate the image. To address this limitation, spatial calibration was achieved by using the 25 gauge cannulas as a reference, since the cannulas had a known outer diameter of 1mm.

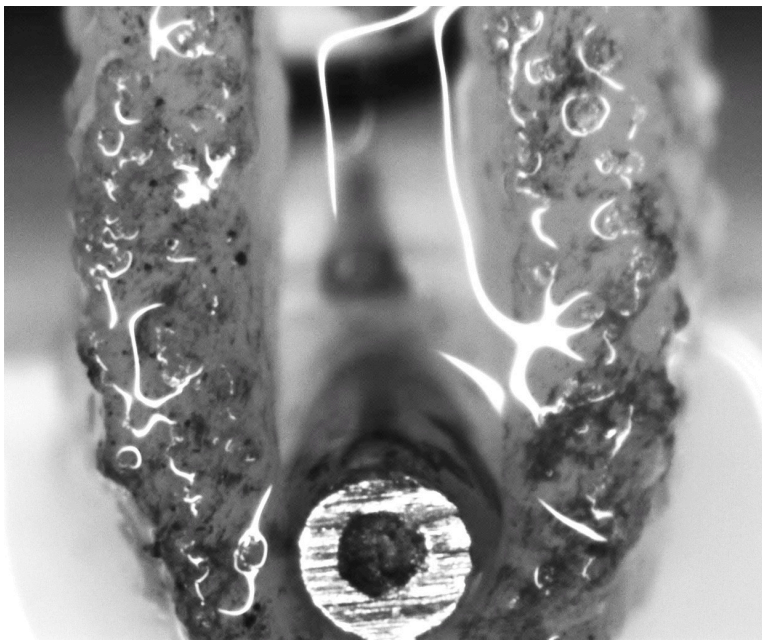

Figure 2.8 Typical speckle pattern for point tracking

Similar testing was performed on samples that had been decellularized using a hypotonic treatment with deionized water followed by a treatment with sodium dodecyl

sulfate (SDS) in Dulbecco's PBS. The constructs were washed in deionized (DI) water for 30 min, stirred continuously in PBS containing 1.0% sodium dodecyl sulfate (SDS) for 60-65h, and rinsed overnight in DI water. They were then rinsed one more time for 30 min, and finally stored in fresh DI water.

2.3 MECHANICAL CHARACTERIZATION

Mechanical testing was performed on ring-shaped tissue constructs that had been cultured between 7 and 17 days in agarose molds. The mechanical response of Cultispher rings was highly repeatable among the test samples (n = 5; outer diameter 4.00-4.17 mm, wall thickness 1.04-1.12 mm, wall height 2.21-2.25 mm) and exhibited a high degree of nonlinearity in the examined range (Figure 2.9). Load and displacement data were processed to yield Cauchy stress σ and axial stretch ratio λ as follows,

$$\sigma = \frac{F}{A_c} \qquad \text{Eq. 2.1}$$

and

$$\lambda = \frac{L_f}{L_0} \qquad \text{Eq. 2.2}$$

where F is the measured load, A_c is the current cross-sectional area, L_f is the current test segment length, L_0 is the initial test segment length, and λ is the axial stretch ratio .

Constant volume was assumed in determining the cross sectional area.

$$V = t * h * L_0 = A_c * L_f \qquad \text{Eq. 2.3}$$

$$A_c = \frac{V}{L_f} \qquad \text{Eq. 2.4}$$

Where V is the volume, t is the specimen thickness, and h is the specimen height.

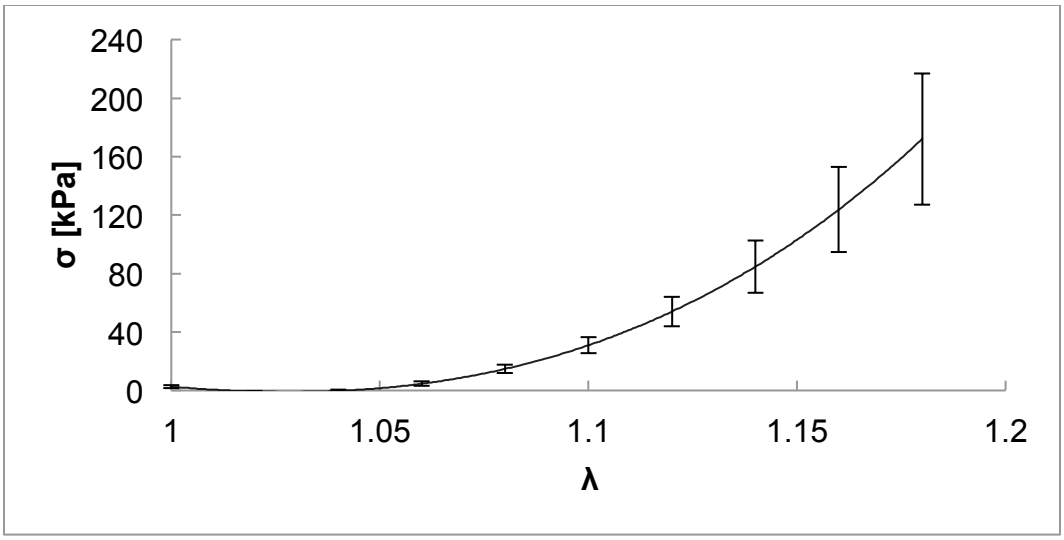

Figure 2.9 Cauchy stress-strain response of tissue ring constructs at 17 days (n=5)

Even though the specimen was ring-shaped, for the purpose of stress/strain analysis it was treated as 2 rectangular posts in tension and data was acquired in the straight regions of the ring that were nominally in uniaxial tension [29]. The length of the specimen was considered to be the distance between 2 points on the straight portion of the specimen when it is mounted onto the cannulas (Figure 2.8). The straight section of the specimen corresponds to the middle third of the specimen, a region that is consistent with recent findings [29]. The initial volume is defined as the initial length of one post multiplied by the height and thickness of the specimen. The current cross sectional area can be determined by dividing the volume by the current length of the post.

In the previous chapter, the arterial mechanical response was modeled using the Holzapfel model. Since parameter identification for the Holzapfel model requires biaxial mechanical test data, and biaxial testing could not be accomplished for the ring specimen, in this study the mechanical response of the ring specimens was modeled using a simple single invariant model [24, 25]. The calibrated single invariant model can be used to make predictions regarding the 3-D response of constructs having different geometry,

most importantly a tube. In future studies, biaxial tests of tubular constructs made from Cultisphers using a similar fabrication method will confirm whether the material parameters found using the uniaxial tests can predict biaxial response.

Basic material assumptions about the mechanical response of the samples were imposed for mechanical modeling. The material was assumed to be elastic, homogeneous, isotropic, and incompressible. Furthermore, it was hypothesized that the strain energy density function W of these materials has the form $W = W(I_1)$, where I_1 is the first invariant of the axial strain tensor calculated as:

$$I_1 = \lambda^2 + \frac{2}{\lambda} \qquad \text{Eq. 2.5}$$

These material assumptions are motivated by the composition and method of preparation of the test samples, and are well-accepted for both synthetic materials that feature long-range molecular order such as rubbers and biological materials such as elastin. It follows that the one-dimensional constitutive equation for such materials is [25]

$$\sigma = [\lambda^2 - \frac{1}{\lambda}][\varphi(I_1, I_2)] \qquad \text{Eq. 2.6}$$

where the non-zero response function φ (I_1, I_2) is

$$\varphi(I_1, I_2) = 2[\frac{dW}{dI_1}] \qquad \text{Eq. 2.7}$$

Simple algebraic manipulation of Eq. 2.6 and 2.7 yields

$$\frac{dW}{dI_1} = \frac{\lambda\sigma}{2(\lambda^3 - 1)} \qquad \text{Eq. 2.8}$$

Linearized plots of $\ln[dW/dI_1]$ versus I_1 can be generated from uniaxial experimental data and reveal the functional form of W (Figure 2.10). The high degree of linear correlation in the resulting plots suggests the following exponential form for W

$$W = \frac{c}{a}(e^{a(I_1 - 3)} - 1) \qquad \text{Eq. 2.9}$$

where c and a are material parameters that can be readily extracted from linear regression (Figure 2.10). Using the parameterized W, theoretical stress versus stretch ratio curves (Figure 2.11) can be generated with the following relation

$$\sigma = 2c\left(\lambda^2 - \frac{1}{\lambda}\right)\exp\left[a\left(\lambda^2 + \frac{2}{\lambda} - 3\right)\right] \qquad \text{Eq. 2.10}$$

Excellent agreement is observed between the experimental and modeled stress response for all samples (Figure 2.11), supporting the proposed mechanical model for Cultispher constructs. The parameters extracted from the model will serve to predict the 3-D biaxial response of tubular constructs. Due to the limitations in the manufacturing process of the tubular construct, biaxial experiments have not yet been conducted to confirm the utility of the model.

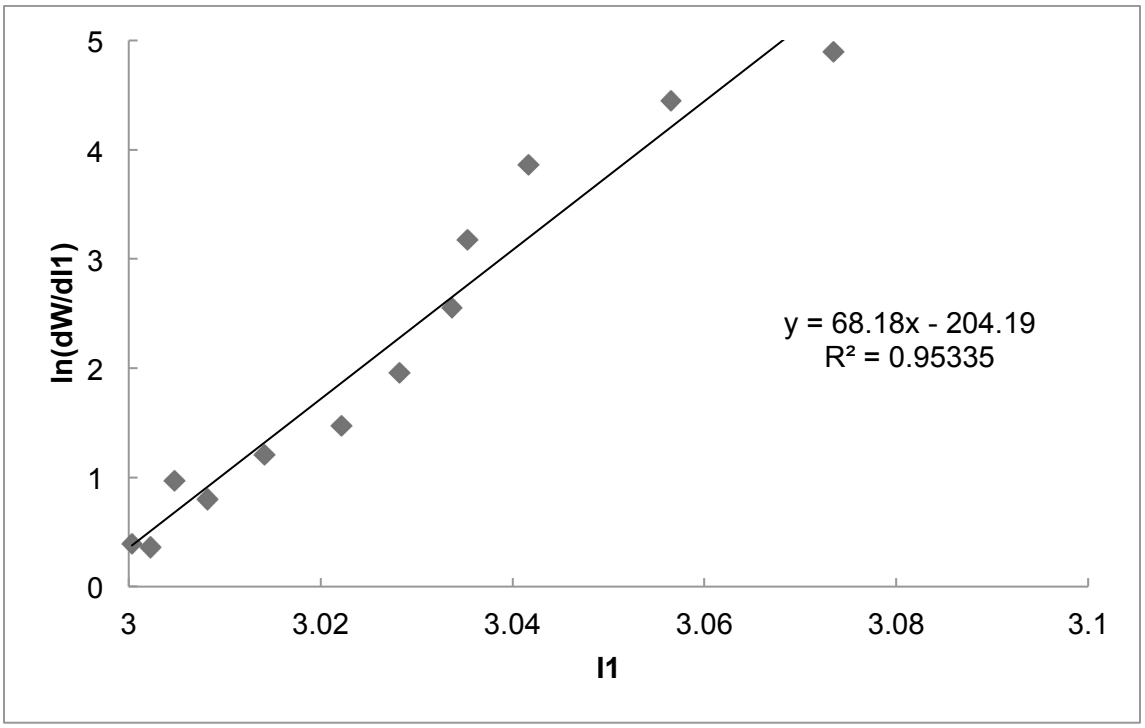

Figure 2.10 Plot of $\ln[dW/dI_1]$ versus I_1 to determine material parameters

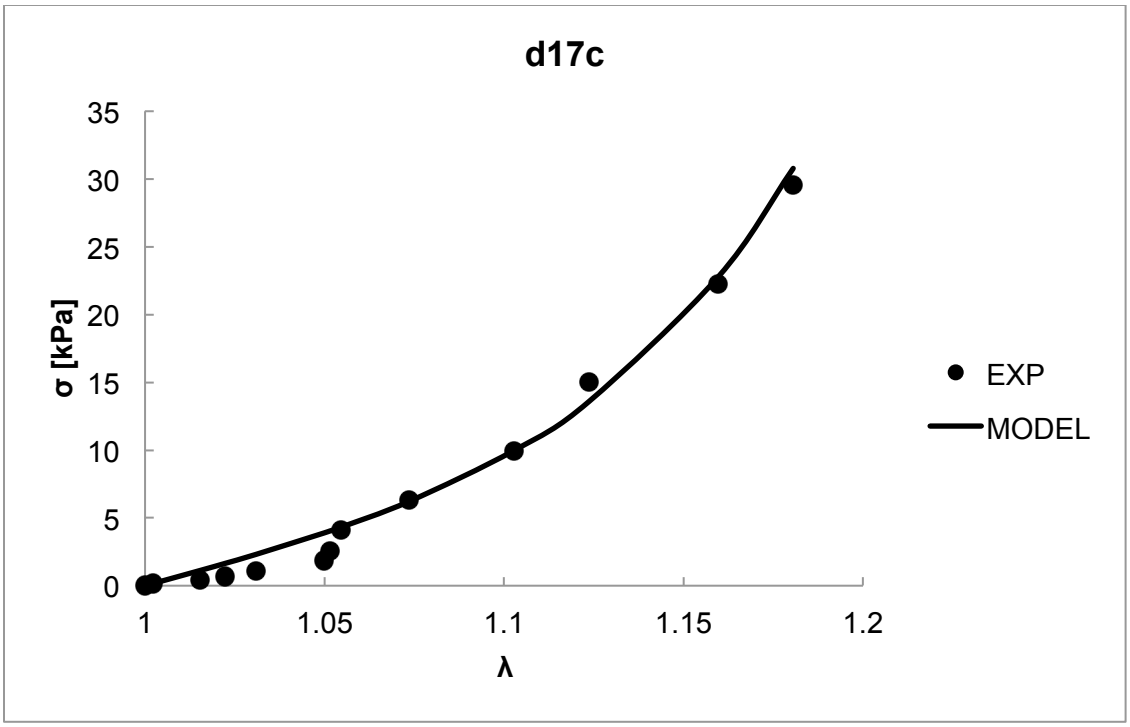

Figure 2.11 Comparison of fitted model response and experimental data

Table 2.1 Fitted Material Parameters for Ring-Construct Tissue Testing

Material Conditions	Sample Number	Mean (a)	Standard deviation	Mean (c) (kPa)	Standard deviation (kPa)
Day 7 cellularized	5	33.8	23.9	0.96	0.48
Day 12 cellularized	5	49.6	24.6	2.2	1.2
Day 17 cellularized	5	51.6	57.3	5.9	5.1
Day 7 decellularized	5	33.9	24.2	4.1	2.1
Day 12 decellularized	5	8.8	8.8	2.0	.77
Day 17 decellularized	5	73.3	23.8	7.6	3.0

Graphs for the Cauchy stress and strain of the cellularized samples as a function of culture time can be seen in Figure 2.12. The sample size was n=5 for each culture period. As can be seen in Figure 2.13, decellularization has a minimal effect on stress response for day 17 constructs. The sample size was n=5 for both cellularized and decellularized constructs.

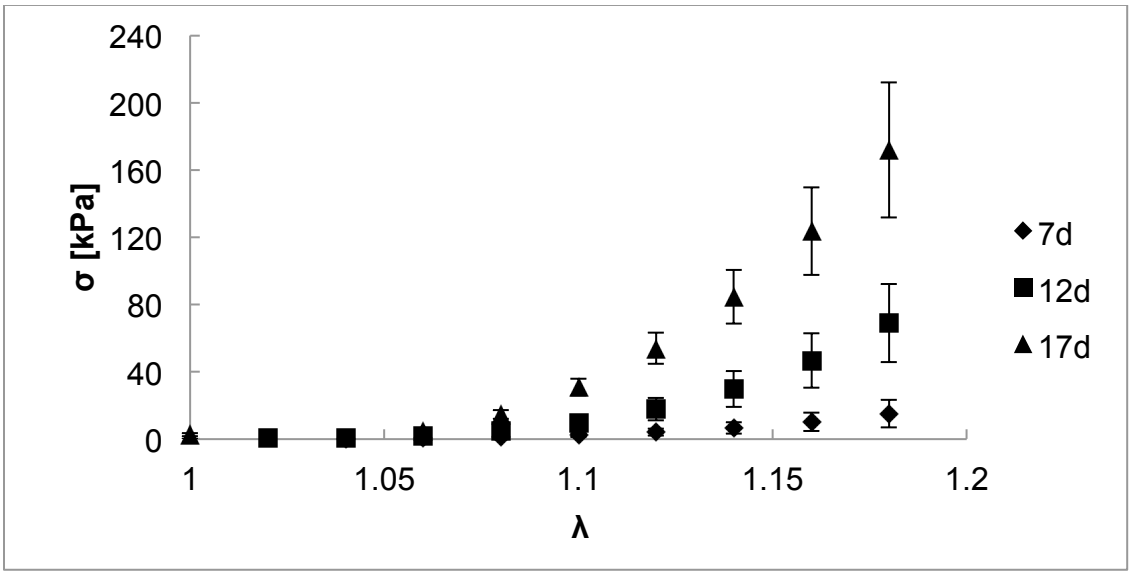

Figure 2.12 Experimental stretch-stress responses of cellularized tissue constructs

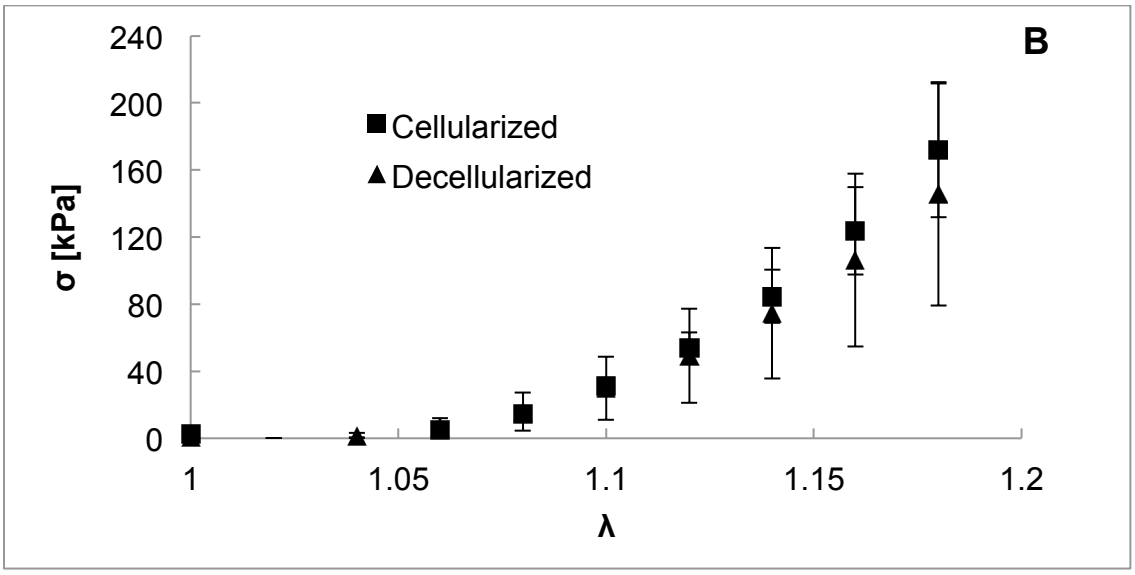

Figure 2.13 Comparison of experimental stretch- stress responses of cellularized and decellularized 17 day constructs

In order to compare the mechanical response of tissue constructs to other tissues in the literature, the elastic moduli for the low strain and high strain region were calculated. It is well-known that native arterial tissues have mechanical properties that are biphasic [22]. The low strain mechanical response is attributed to the extension of elastin fibers and the high strain mechanical response is attributed to the extension of collagen fibers [30]. In our case, the engineered tissue constructs show similar behavior, with an elastin dominant phase, a transition region, and a collagen dominant phase. For this reason, we calculated incremental elastic moduli based on the linear portion of the low strain region (elastin) and the high strain (collagen) region. Using our sample data, the different phases can be seen in Figure 2.14.

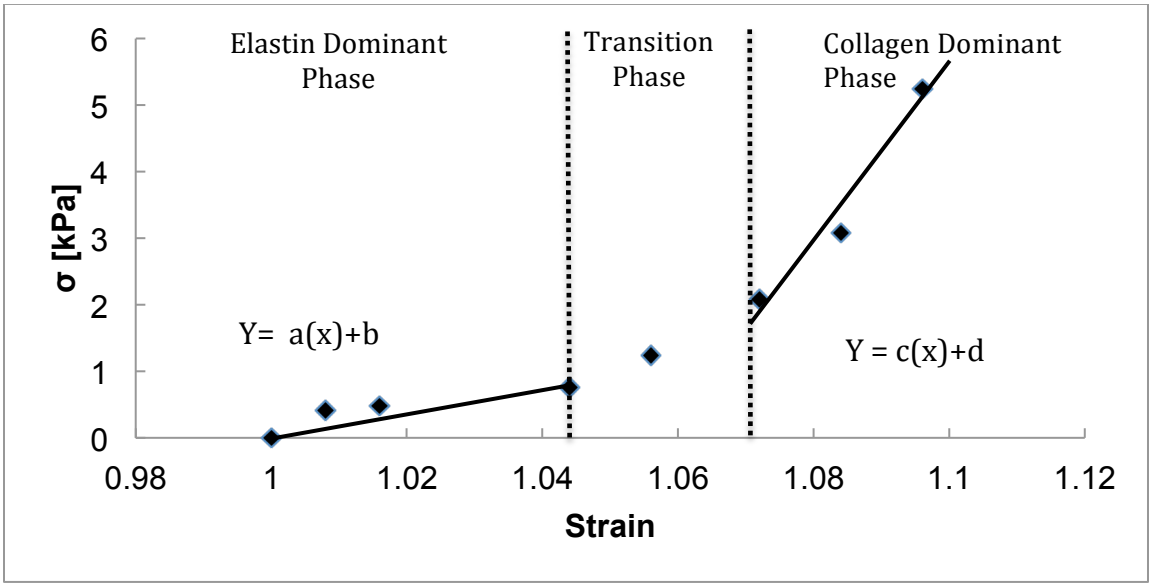

Figure 2.14 Elastin dominant phase, transition phase, and collagen dominant phase of ring-shaped tissue constructs

To determine the incremental elastic moduli of the elastin- and collagen-dominant phases, the experimental data were linearized as seen in Figure 2.14. Table 2.2 summarizes the incremental elastic moduli of collagen- and elastin-dominant phases for culture times between 7 and 17 days.

As seen in Table 2.2, Figure 2.15, and Figure 2.16, the average incremental elastic modulus for collagen and elastin dominant regions increased with increasing culture time for the cellularized samples. We expected to see the same trend with the decellularized samples considering the decellularization process had negligible effect on mechanical response (Figure 2.13). As evidenced by the data below, we saw a decrease in elastin modulus for the decellularized samples between the day 7 and day 12 time points. In all cases, except day 12 decellularized, all the ring-shaped constructs with the same culture time were cultured simultaneously. For example, when the day 7 rings reached the end of their culture time, 5-7 ring specimens were used for cellularized tests, and the rest were subjected to decellularization prior to mechanical testing. For the day 12 samples, the cellularized and decellularized samples were not from the same batch. For this reason, we believe the difference in donor smooth muscle cells was the reason for lack of mechanical integrity in the day 12 decellularized constructs.

Table 2.2 Incremental Elastic Moduli and Ultimate Tensile Strength of Ring Constructs

Material Conditions	Sample Number	E-Elastin [kPa]	E-Collagen [kPa]	Ultimate Tensile Strength
Day 7 Cellularized	5	5.88 +/- 4.16	43.05 +/- 33.90	15.12 +/- 2.59
Day 12 Cellularized	5	17.42 +/- 13.52	231.14 +/- 90.81	33.99 +/- 8.42
Day 17 Cellularized	5	34.67 +/- 15.37	268.52 +/- 229.94	47.08 +/- 6.21
Day 7 Decellularized	5	20.63 +/- 13.66	120.55 +/- 84.88	11.58 +/- 0.86
Day 12 Decellularized	5	8.88 +/- 5.56	28.89 +/- 15.60	35.62 +/- 9.57
Day 17 Decellularized	5	114.32 +/- 116.49	575.36 +/- 358.48	37.15 +/- 6.44

All data was subjected to a one-way ANOVA with Tukey's post-hoc analysis, where $p < .05$ was considered significant.

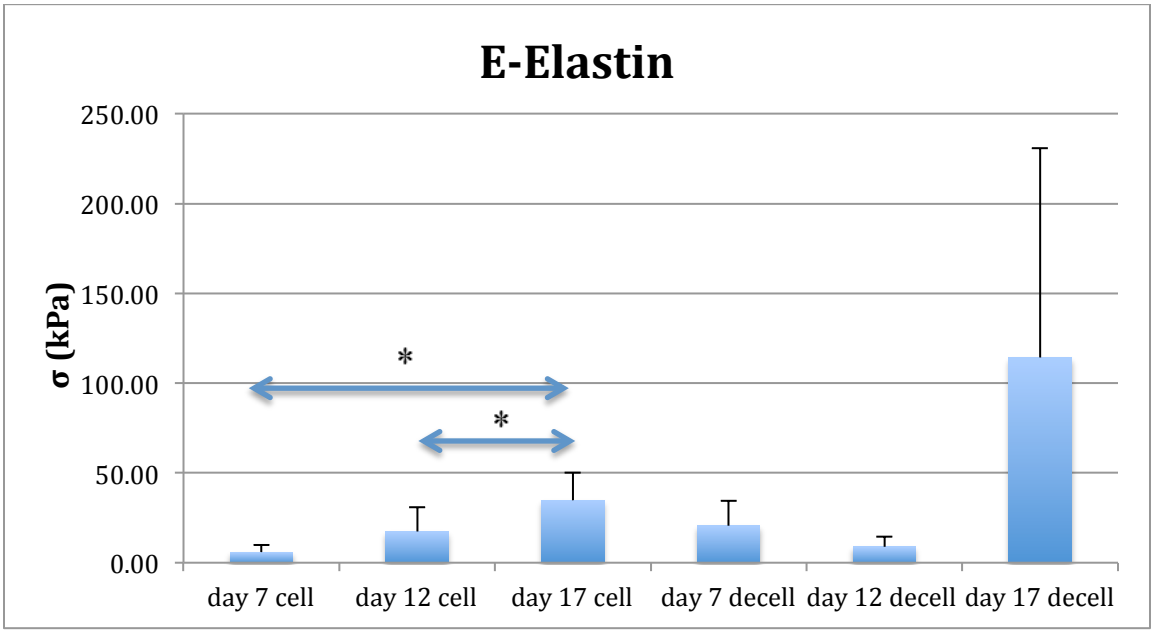

Figure 2.15 Incremental elastic modulus of elastin-dominant phase for cellularized (cell) and decellularized (decell) samples

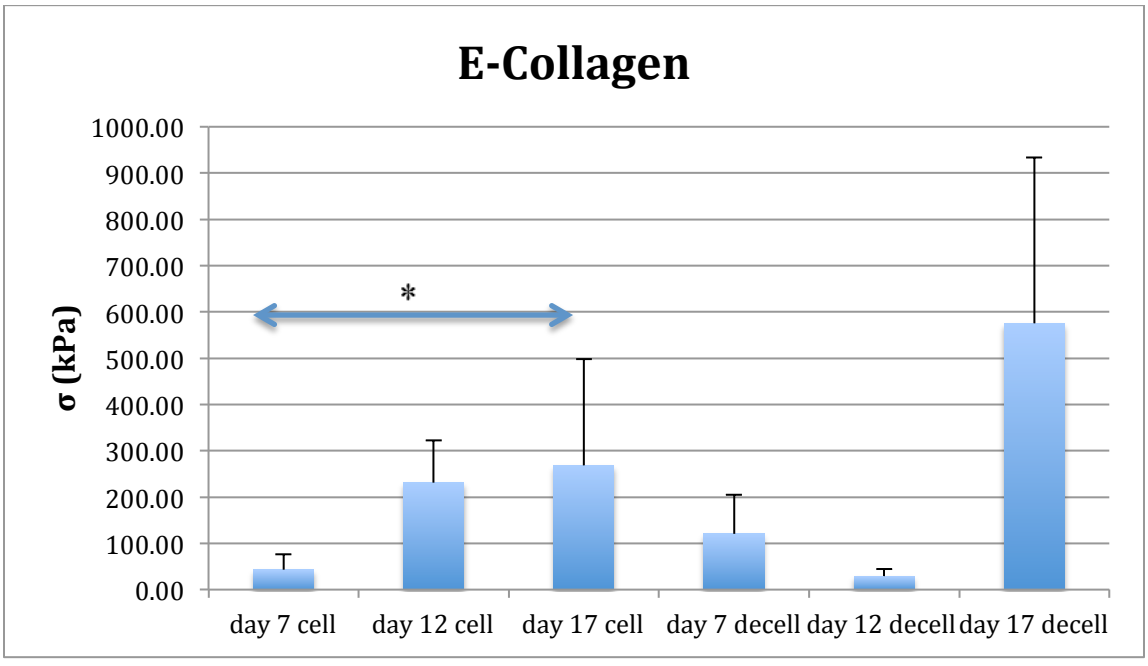

Figure 2.16 Incremental elastic modulus of collagen-dominant phase for cellularized (cell) and decellularized (decell) samples

Ultimate tensile strength was measured by increasing strain until the maximum load was recorded before sample failure. Data for the ultimate tensile strength can be seen in Figure 2.17.

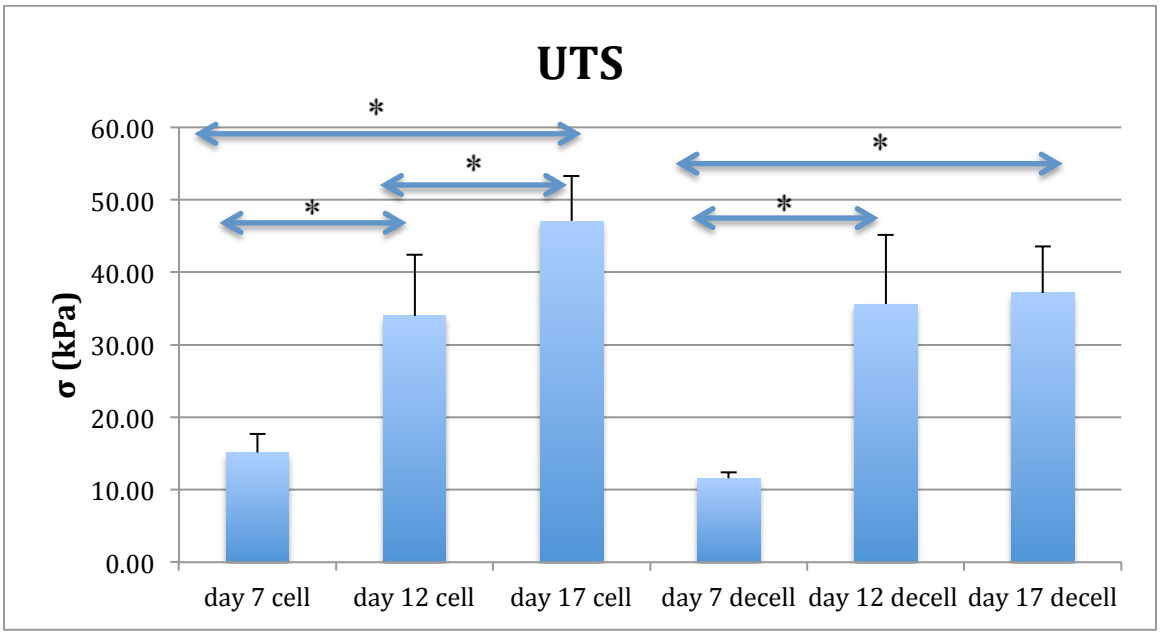

Figure 2.17 Ultimate tensile strength of cellularized (cell) and decellularized (decell) samples

As seen in Figure 2.17, the average ultimate tensile strength significantly increased with increasing culture time for the cellularized samples. There was no significant change between the day 12 and day 17 decellularized samples; however, there was a significant increase between day 7 and day 17 for the decellularized samples.

To determine whether static internal circumferential stretch has an effect on the tissue specimens, special posts were made for stretching the specimens after the initial 7-day culture period. It has been shown that HUVECs and HASMCs respond to mechanical stimulus by remodeling the extracellular matrix [25]. Wagenseil *et al.*(2010) showed that elastin production results directly from mechanical forces imparted on blood vessels during normal vessel development.

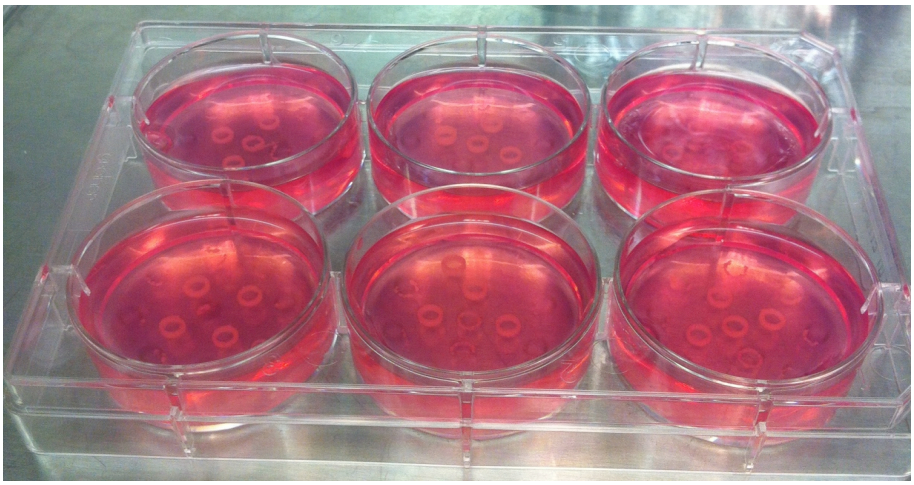

Figure 2.18 Ring specimen on 2mm agarose posts in molds

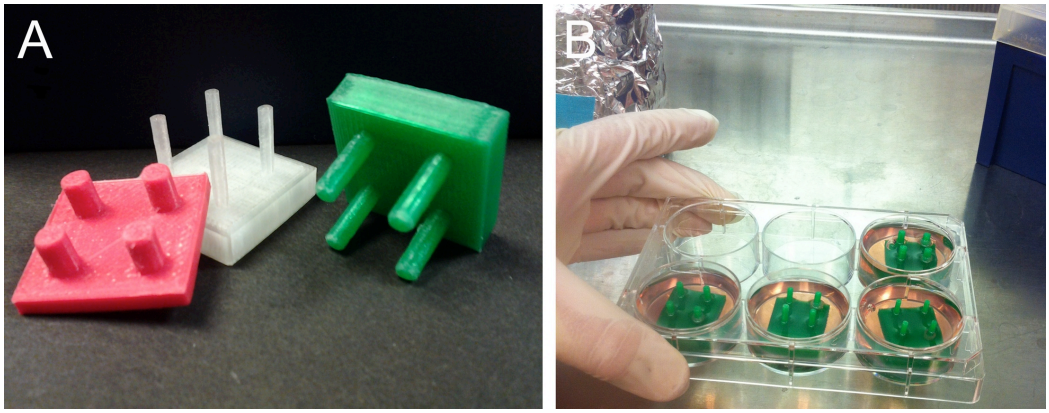

Figure 2.19 Fabricated PLA posts to initiate static circumferential strain

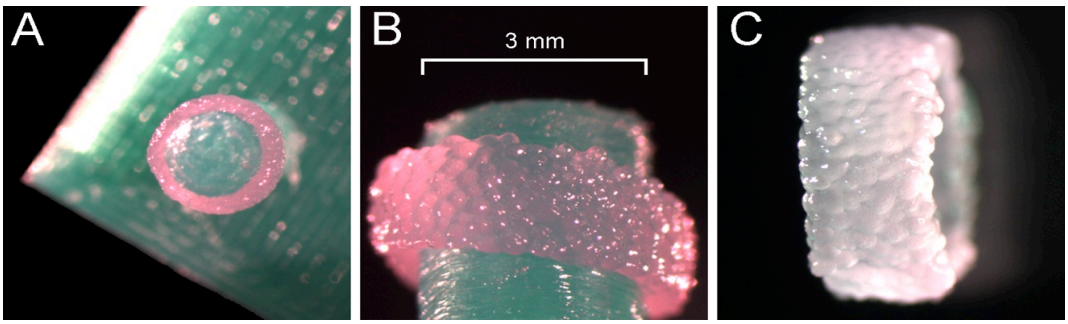

Figure 2.20 Close up of ring specimen on 3mm PLA posts

In this study, after 5 days of culture in agarose molds with 2mm luminal posts (Figure 2.18), the ring specimens were removed from the molds. Immediately following

removal, the ring specimens were placed on special bio-inert posts made from polylactic acid (PLA) for the remainder of the 12 day culture time (Figures 2.19 and 2.20).

Day 12 cellularized ring specimens on 2mm agarose posts in molds were used as the control and day 12 cellularized ring specimens on PLA posts of 2mm and 3mm were tested to examine how experimental conditioning parameters influence the mechanical or morphological outcomes of these structures. Ring specimens that were cultured on 2mm PLA posts were compared to ring specimens cultured on 2mm agarose posts to determine whether any changes were attributed to the change of culture environment and boundary conditions. Ring specimens of 3mm were subjected to 50% static circumferential strain and compared to the 2mm agarose and PLA cultured ring specimens to determine the effect of static strain.

Before mechanical loading experiments were conducted, sample geometry was recorded for each specimen after removal from the posts. A relaxation time of at least one minute after removal was permitted to allow the specimen to reach its resting geometry and to allow for the application of the dot pattern. It was interesting to find significant changes in geometry between the different culture conditions. Summarized data comparing changes in geometry of the ring specimens can be seen below in Table 2.3.

Table 2.3 Geometric Parameters of Statically Strained Specimens

Material Conditions	Sample Number	Inner Diameter (mm)	Thickness (mm)	Outer Diameter (mm)
2mm Agarose Post	18	2.31 +/- 0.27	0.72 +/- 0.09	3.79 +/- 0.16
2mm PLA Post	17	1.89 +/- 0.35	0.96 +/- 0.19	3.83 +/- 0.21
3mm PLA Post	17	2.41 +/- 0.42	0.88 +/- 0.22	4.20 +/- 0.29

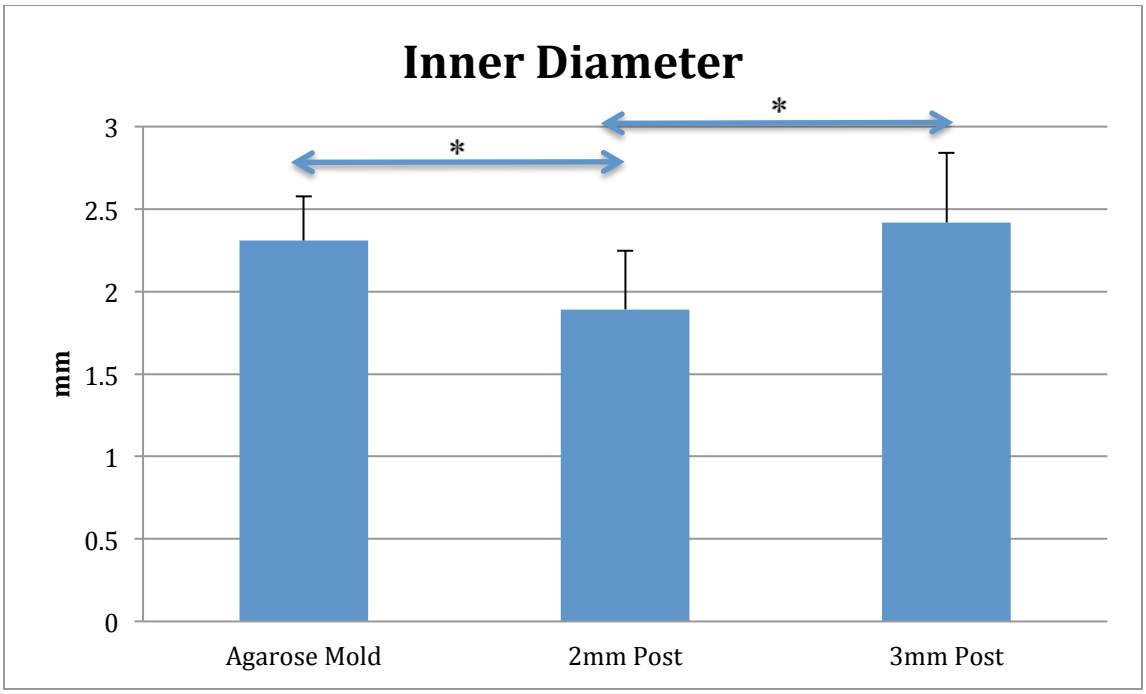

Figure 2.21 Comparing inner diameter of stretched and unstretched ring specimens

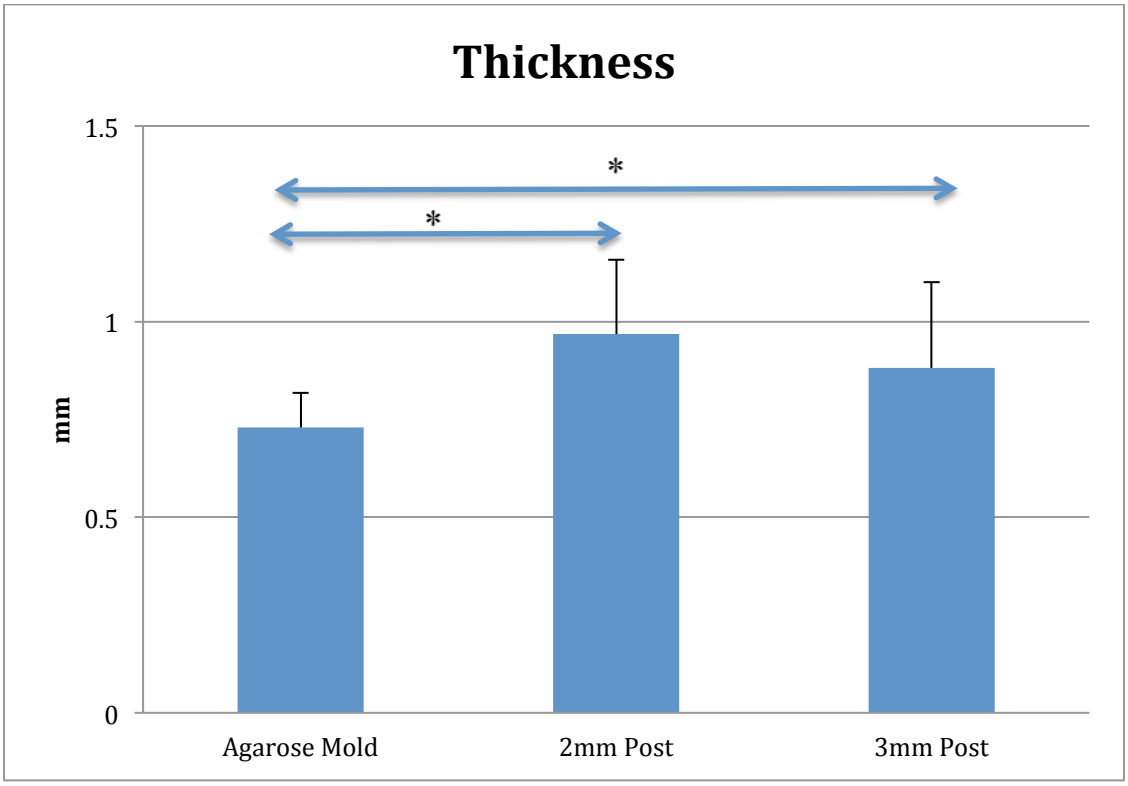

Figure 2.22 Comparing thickness of stretched and unstretched ring specimens

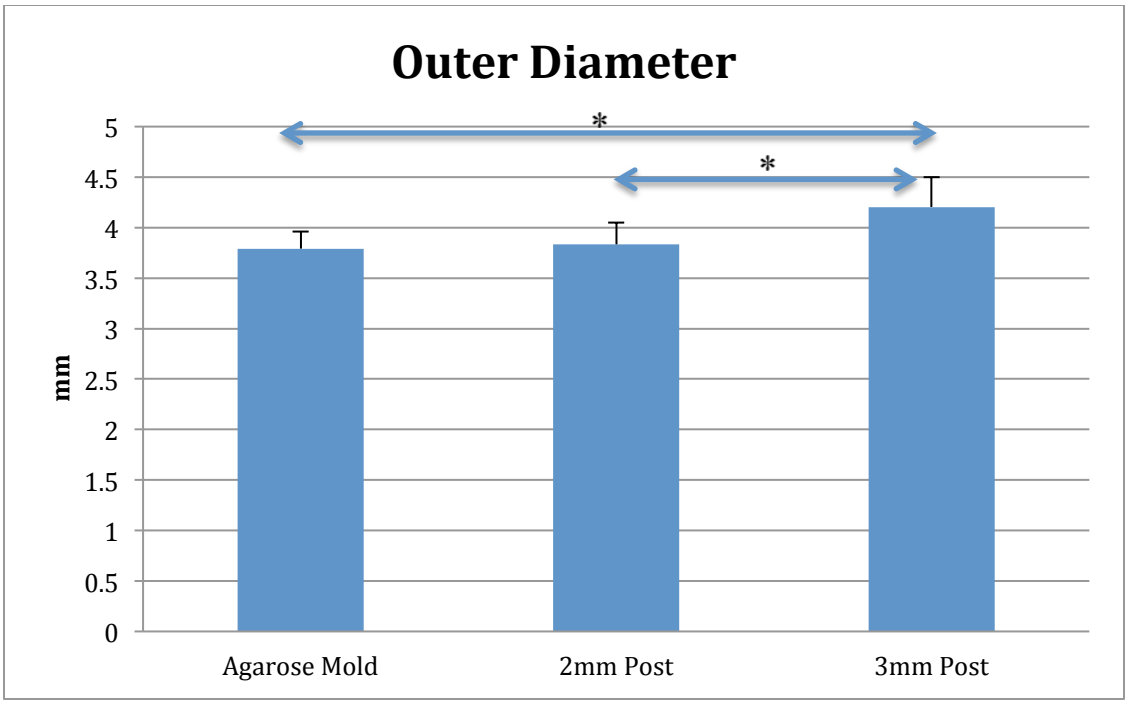

Figure 2.23 Comparing outer diameter of stretched and unstretched ring specimens

Mechanical testing of statically strained ring constructs and controls was conducted as mentioned previously in Section 2.3. Summarized data comparing the mechanical response of the ring specimens can be seen below in Table 2.4.

Table 2.4 Elastic Modulus and Ultimate Tensile Strength of Statically Strained Specimens

Material Conditions	Sample Number	E-Elastin (kPa)	E-Collagen (kPa)	Ultimate Tensile Strength
2mm Agarose Post	5	12.42 +/- 13.52	231.14 +/- 90.81	33.99 +/- 8.42
2mm PLA Post	5	27.68 +/- 21.53	228.54 +/- 99.16	40.78 +/- 3.93
3mm PLA Post	5	25.15 +/- 13.11	406.17 +/- 120.33	40.01 +/- 10.18

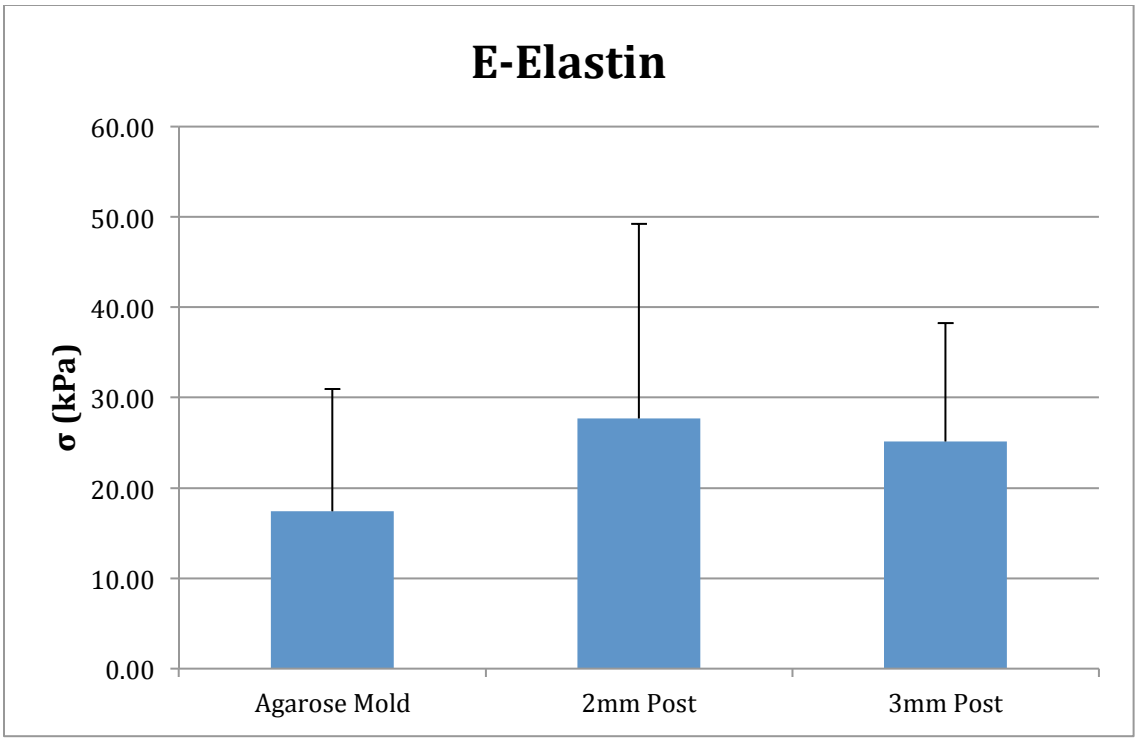

Figure 2.24 Comparing incremental elastic modulus of elastin dominant region for stretched and unstretched ring specimens

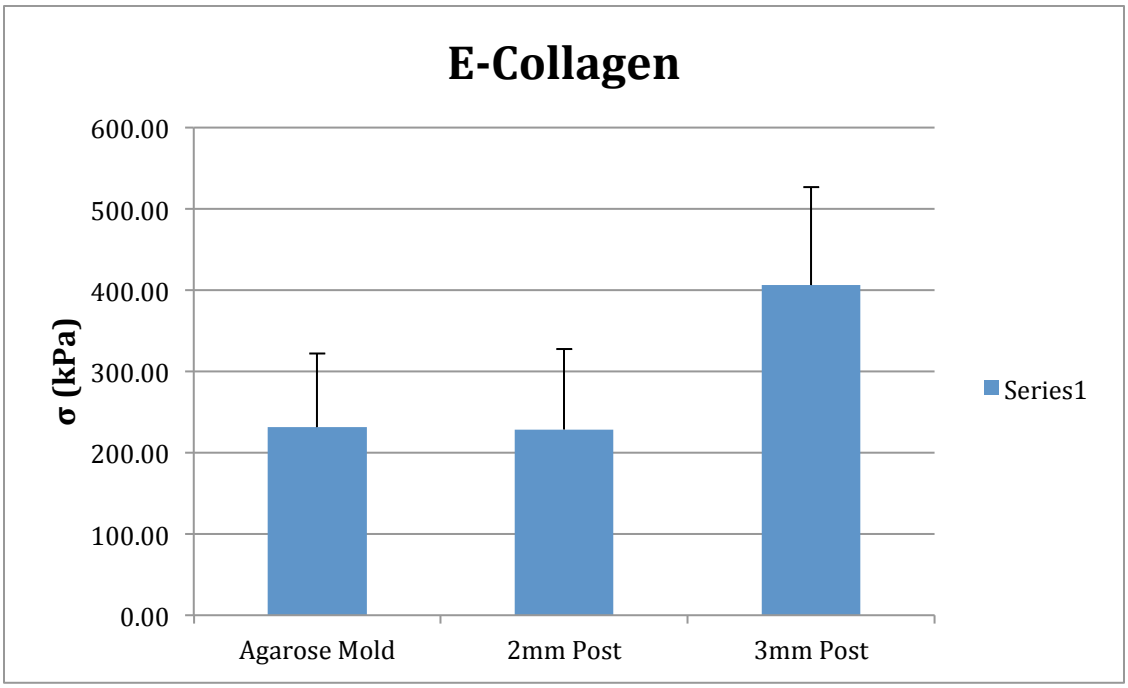

Figure 2.25 Comparing incremental elastic modulus of collagen dominant region for stretched and unstretched ring specimens

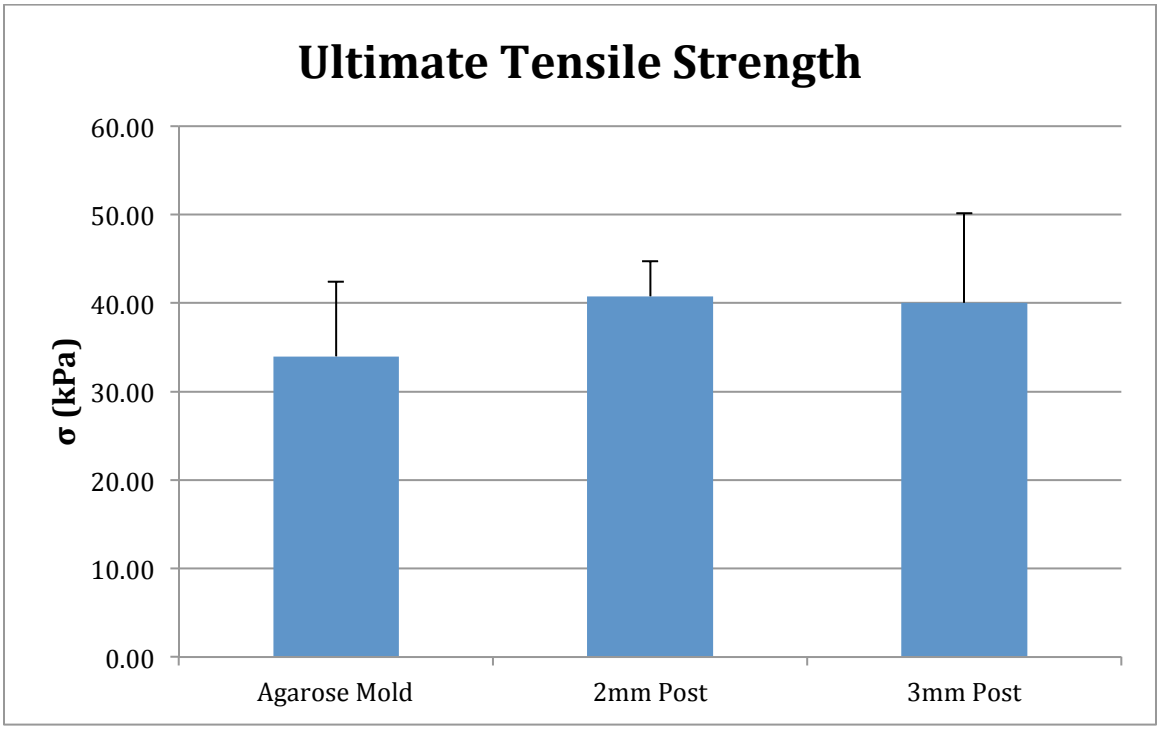

Figure 2.26 Comparing ultimate tensile strength for stretched and unstretched ring specimens

3.4 CONCLUSION

We have characterized the uniaxial mechanical response of ring-shaped constructs formed by self-adhesion of cellularized gelatin macroporous microcarriers ('Cultispheres'). Stress-strain response of ring shaped Cultispher constructs exhibit a nonlinear elastic mechanical response to uniaxial extension, characterized by increased stiffness at higher stretch ratios. The specimens exhibited mechanical behavior that could be analyzed as biphasic. Therefore, incremental elastic moduli for low strain and high strain regions were examined, and the findings demonstrate that the constructs increased in elastic modulus as culture time increased. The study shows that the tissue constructs maintain mechanical integrity following the decellularization process. These findings suggest that this approach could be used to produce "off the shelf" tissue constructs that

exhibit mechanical responses that are controlled by culture time. Biomechanical testing of the constructs demonstrated mechanical behavior consistent with that of an isotropic, incompressible, homogeneous, elastic material that could be modeled using a simple single invariant material model. Studies show excellent agreement between experimental stress strain response and modeled stress strain response. The effect of static strain was also examined, and it was found that static stretch during culture did not have an effect on the mechanical response. However, we did find significant differences between morphologies of statically strained and unstrained constructs.

CHAPTER 3

FUTURE WORK

3.1 RENAL ARTERY

Histological studies were conducted to determine the area fraction of collagen and elastin in the renal and branch arteries. Future work will include determining the percent of smooth muscle cells (SMCs) that are in the specimens to see if there is a difference in composition. To determine specifically the constituents of our material, SMC area fractions need to be determined to include in our model. SMC content is also important to examine in the study of active mechanics. In this paper, all tests were conducted on passive arteries, meaning there was no contribution of SMC contraction to mechanical responses. In active mechanics, epinephrine is used to stimulate SMC contraction, and comparisons can be drawn between the active and passive mechanics. It is important to conduct passive tests because they serve as a baseline for the active tests. The contribution of the active response is determined by subtracting the contribution of the passive response.

In our Holzapfel-type constitutive model, 4 parameters could not be calculated because the appropriate tests were not conducted. In future work, tests on arteries must include axial extension tests on renal arteries at zero pressure. In this study, the smallest pressure studied was 20mmHg.Lastly, we would like to histologically determine the average collagen fiber angle in the renal artery and compare it to that of the first branch.

Second harmonic generation (SHG) microscopy could be used to determine this average collagen fiber angle. The Holzapfel model described in chapter 1 was able to make predictions about the average collagen fiber angles for the renal artery and the first branch, and it is important to confirm these values with histological data.

3.2 NEWLY DEVELOPED TISSUE CONSTRUCT

Point tracking was used to determine the average axial strain as described in Chapter 2. This method was sufficient for this study; however, to better understand local strain variations, a full field digital image correlation (DIC) technique needs to be implemented. In this study, the dot pattern used for strain tracking was applied by hand using a cotton tip applicator and blue tissue marking dye. We are currently working on a nuclear staining technique using Triton-X permeabilization and ethidium bromide to get a better full field analysis of the strain. As seen below in Figure 3.1, the light colored "dots" are nuclei that are stained. These nuclei will be used to track the tissue strain in the deformed state.

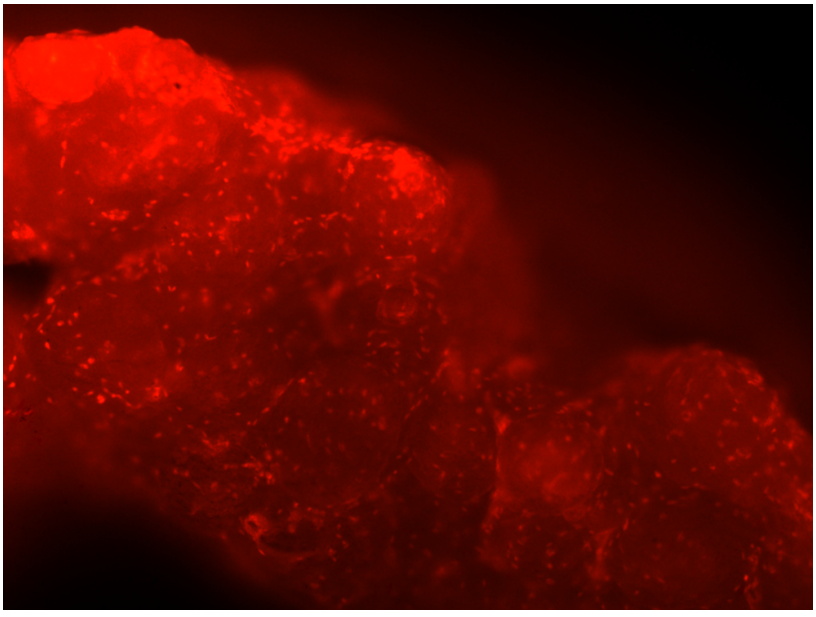

Figure 3.1 Ethidium bromide staining of tissue ring specimen

In this study, the effect of static strain during tissue ring culture was examined and found not to have a significant influence on mechanical strength. However, in the literature it is shown that mechanical forces influence collagen and elastin production. In the static strain study, constant circumferential stresses were applied. This allowed the material to remodel to minimize stress. In future work, we would like to examine the effect of dynamic strain and loading on the ring specimens. A bioreactor has been designed that will allow for dynamic loads to be applied during culture (Figure 3.2 and 3.3). Future studies will examine the effect of dynamic loads on elastin and collagen production, as well as on specimen morphology.

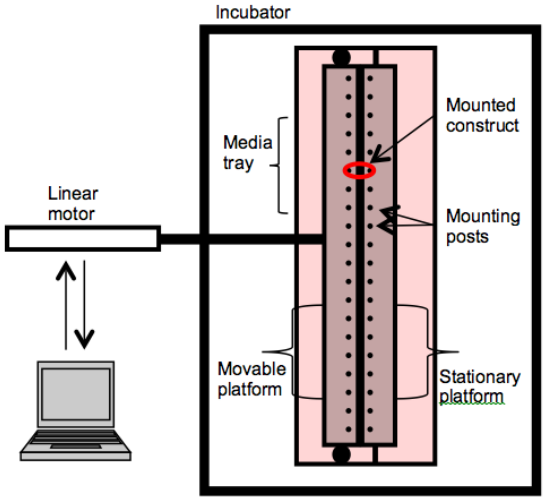

Figure 3.2 Schematic of dynamic loading bioreactor

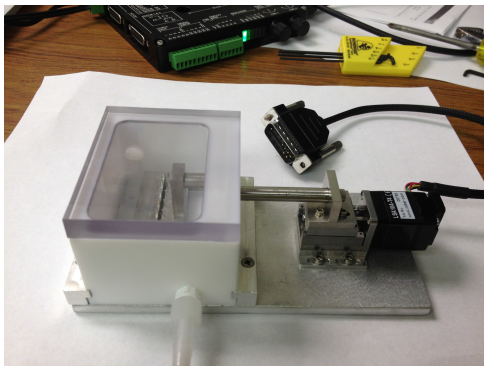

Figure 3.3 Dynamic loading bioreactor

In this study, the ring specimens were modeled using a single invariant material model. This model has utility in being able to predict 3-D biaxial response of a tube shaped specimen by using data from a uniaxial ring test. The predictions from this model have yet to be validated by testing a tubular specimen. In order to have utility as a vascular replacement, tube shaped specimens must be developed. In future work, our collaborators will provide tubular constructs that will be tested under the same conditions as the renal arteries in chapter 1. Preliminary testing of tube shaped specimens can be seen below in Figure 3.4.

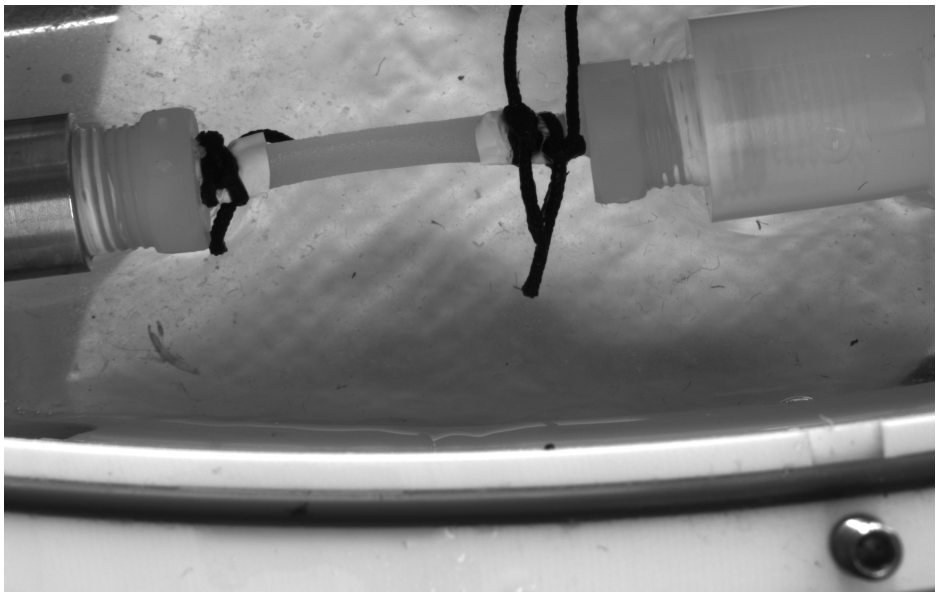

Figure 3.4 Tubular specimen undergoing tension-inflation biaxial test

REFERENCES

[1] M. Alan S. Go, M. D. F. Dariush Mozaffarian and M. M. F. Véronique L. Roger. Heart Disease and Stroke Statistics -2013 Update : A Report from the American Heart Association. Journal of The American Heart Association, pp. e6-e245, 2013.

[2] A. G. Kalamas and C. U. Niemann. Patients with Chronic Kidney Disease. Medical Clinics of North America, pp. 1109-1122, 2013.

[3] W.O Twal, SC Klatt, K Harikrishnan, E Gerges, MA Cooley, TC Trusk, B Zhou, M Gabr, T Shazly, SM Lessner, RR Markwald, WS Argraves. Cellularized Microcarriers as Adhesive Building Blocks for Fabrication of Tubular Tissue Constructs. Ann Biomed Eng. 2013.

[4] Cardamone, L., A. Valentín, J.F. Eberth, J.D. Humphrey. Origin of axial prestretch and residual stress in arteries. Biomech Model Mechanobiol. 8(6):431-446, 2009.

[5] Van Loon, P., W. Klip, E.L. Bradley. Length–force and volume–pressure relationships of arteries. Biorheology 14:181–201, 1977.

[6] Brossollet, L.J., R.P. Vito. An alternate formulation of blood vessel mechanics and the meaning of the in vivo property. J. Biomech. 28:679–687, 1995.

[7] Avril S, Badel P, Gabr M, Sutton MA, Lessner SM. Biomechanics of Porcine Renal Artery and Role of Axial Stretch. J Biomech Eng. 2013 Aug;135(8):81007. doi: 10.1115/1.4024685.

[8] Holzapfel, G.A., Gasser, T.C., Ogden, R.W., 2000. A new constitutive framework for arterial wall mechanics and a comparative study of material models. J. Elast. 61, 1–48.

[9] Holzapfel, G.A. Determination of material models for arterial walls from uniaxial extension tests and histological structure. J. Theor. Biol. 238:290–302, 2006.

[10] Humphrey, J.D., J.F. Eberth, W.W. Dye, R.L. Gleason. Fundamental role of axial stress in compensatory adaptations by arteries. J. Biomech. 42:1–8, 2009

[11] Weizsacker, H.W., H. Lambert, K. Pascale. Analysis of the passive mechanical properties of rat carotid arteries. J. Biomech. 16:703–715, 1983.

[12] Desai, M., A. M. Seifalian, and G. Hamilton. Role of prosthetic conduits in coronary artery bypass grafting. Eur. J. Cardiothorac. Surg. 40(2):394–398, 2011.

[13] Borschel, G. H., Y. C. Huang, S. Calve, E. M. Arruda, J.B. Lynch, D. E. Dow, W. M. Kuzon, R. G. Dennis, and D.L. Brown. Tissue engineering of recellularized small diameter vascular grafts. Tissue Eng. 11(5–6):778–786, 2005.

[14] L'Heureux, N., S. Paquet, R. Labbe, L. Germain, and F. A. Auger. A completely biological tissue-engineered human blood vessel. FASEB J. 12(1):47–56, 1998.

[15] Mitchell, S. L., and L. E. Niklason. Requirements for growing tissue-engineered vascular grafts. Cardiovasc. Pathol. 12(2):59–64, 2003.

[16] Buttafoco, L., P. Engbers-Buijtenhuijs, A. A. Poot, P. J. Dijkstra, I. Vermes, and J. Feijen. Physical characterization of vascular grafts cultured in a bioreactor. Biomaterials
27(11):2380–2389, 2006.

[17] Hibino, N., E. McGillicuddy, G. Matsumura, Y. Ichihara, Y. Naito, C. Breuer, and T. Shinoka. Late-term results of tissue-engineered vascular grafts in humans. J. Thorac. Cardiovasc. Surg. 139(2):431–436, 2010; 436:e431–e432.

[18] Hirtenstein, M., J. Clark, G. Lindgren, and P. Vretblad. Microcarriers for animal cell culture: a brief review of theory and practice. Dev. Biol. Stand. 46:109–116, 1980.

[19] Nikolai, T. J., and W. S. Hu. Cultivation of mammalian cells on macroporous microcarriers. Enzyme Microb. Technol. 14(3):203–208, 1992.

[20] Martin, Y., M. Eldardiri, D. J. Lawrence-Watt, and J. R. Sharpe. Microcarriers and their potential in tissue regeneration. Tissue Eng. Part B, Rev. 17(1):71–80, 2011.

[21] Clavijo-Alvarez, J. A., V. T. Nguyen, L. Y. Santiago, J. S. Doctor, W. P. Lee, and K. G. Marra. Comparison of biodegradable conduits within aged rat sciatic nerve defects. Plast. Reconstr. Surg. 119(6):1839–1851, 2007.

[22] W.S.Sheridan, G.P.Duffy, B.P. Murphy, "Mechanical characterization of a customized decellularized scaffold for vascular tissue engineering", Journal of the Mechanical Behavior of Biomedical Materials, 2011.

[23] A. Rachev, T. ElShazly, and D. N. Ku. "Constitutive formulation of mechanical properties of synthetic hydrogels," ASME International Mechanical Engineering Congress, Nov. 13-19, 2004, Anaheim, CA, USA.

[24] T. ElShazly, 2004. Characterization of PVA Hydrogels with Regards to Vascular Graft Development. MS Thesis, Georgia Institute of Technology, Atlanta, GA.

[25] Wagenseil J.E., Mecham R.P. Vascular extracellular matrix and arterial mechanics. Physiol Rev. 2009;89:957–989.

[26] X Zhao, HS Zhang, MA Sutton, AP Reynolds, X Deng, HW Schreier and X Ke. Stereo Image Based Particle Tracking in Fluids: Experimental Validation and Application to Friction Extrusion Process Model. Experimental Mechanics (in review).

[27] X. Ke, M.A. Sutton, S. Lessner and H.W. Schreier, Robust stereovision and calibration methodology for accurate 3D digital image correlation measurements on submerged objects, Journal of Strain Analysis for Engineering Design 43 689-704 (2008).

[28] Sutton, M.A, C. McFadden, Development of a methodology for non-contacting strain measurements in fluid environments using computer vision, Optics and Lasers in Engineering, 32, 367-377 (2000).

[29] Shazly T., Rachev A., Lessner S.M., Argraves W.S., Ferdous J, Zhou B, Sutton M.A. On the mechanical response of soft tissues under uniaxial loading. Experimental Mechanics. 2013

[30] Roach, M. R., and A. C. Burton. The reason for the shape of the distensibility curves of arteries. Can. J. Biochem. Physiol. 35(8):681–690, 1957